Chapter 3

Detector and Monte Carlo

The bored tourists who pay their nine francs at the desk or are admitted free on Sundays may believe that elderly nineteenth-century gentlemen — beards yellowed by nicotine, collars rumpled and greasy, black cravats and frock coats smelling of snuff, fingers stained with acid, their minds acid with professional jealousy, farcical ghosts who called one another cher maître — placed these exhibits here out of a virtuous desire to educate and amuse the bourgeois and the radical taxpayers, and to celebrate the magnificent march of progress. But no...

U. Eco, "Foucault's Pendulum"

3.1 The Tevatron

The search for anomalous $ZV\gamma$ couplings requires high energies for the interacting particles. The Fermi National Accelerator Laboratory high luminosity proton-antiproton collider (Tevatron) with a center of mass energy of 1.8 TeV made it possible for the first time to study these couplings in hadronic collisions. This section contains a brief description of the accelerator and its main operating principles. More details on the Tevatron accelerator can be found in [49, 50].

3.1.1 Historical Sketch

The state-of-art Tevatron accelerator complex currently provides the highest energy proton and antiproton beams in the world, and most likely will remain the most powerful $p\bar{p}$ collider at least until the beginning of the next century. The existence of this machine became possible due to a number of important achievements in accelerator techniques, such as antiproton cooling and storage, developed at CERN [51], superconductor manufacturing and technology, detailed computer simulation of beam behavior, and many others. The Tevatron is truly the top of the line of the modern accelerators.

The machine was built in several steps. It started in 1970 with the installation of the 200 MeV high-current linear accelerator (Linac) [52]. From 1972 to 1982 the 8 GeV booster and the Main Ring [53] (typically running at 400 GeV energy) were built. The fixed target physics program at 400 GeV was conducted at Fermilab from the mid-70's through January 1984. During that time the superconducting Tevatron ring (then known as the Energy Doubler) [49] was installed in the Main Ring tunnel, and after a short shutdown the first 800 GeV fixed target run took place in July 1984, followed by the second similar run in 1985. The antiproton source [54] was commissioned in July 1985, and on October 12, 1985, the first Tevatron $p\bar{p}$ collisions were seen in the CDF detector. The first, low luminosity ($\sim$ 4 pb^{-1}), Tevatron run took place in 1988 – 1989 with only the CDF detector collecting physics data. During a three year shutdown another fixed target run was conducted, the accelerator system was improved, and the DØ detector was assembled and prepared for the first, high-luminosity ($\sim$ 20 pb^{-1}), run which took place from August 1992 through May 1993 (run Ia).

3.1.2 Tevatron Operation in Collider Mode

The Tevatron accelerator complex consists of several separate parts shown in Fig. 3.1. The Cockroft-Walton accelerator is used for initial acceleration of H^- ions obtained by ionizing hydrogen gas with electrons. This small accelerator uses a static electric field to accelerate ions to an energy of 750 keV. The ions are then transported to a 150 meter long Linac which accelerates them to $200 - 400$ MeV and shoots the beam through a carbon foil which strips off the electrons from the hydrogen ions leaving only protons in the beam. During the next stage, the protons are accelerated to 8 GeV in a small (500 meters in circumference) synchrotron ring (the Booster) and injected into the Main Ring (which is also a synchrotron), located in the tunnel with a circumference of 3.7 miles, or more than 6000 meters. The Main Ring consists of over 1000 conventional warm temperature copper-coiled magnets. The proton beam in the Main Ring is accelerated to $\sim$ 120 GeV and formed into a set of short bunches with $\sim 2 \cdot 10^{12}$ protons per bunch. The bunches can be either transported into the superconducting Tevatron ring (in order to fill it with a proton store), or dumped on a nickel/copper target (located in the Target Hall), producing $\sim 2 \cdot 10^{7}$ antiprotons per proton bunch.

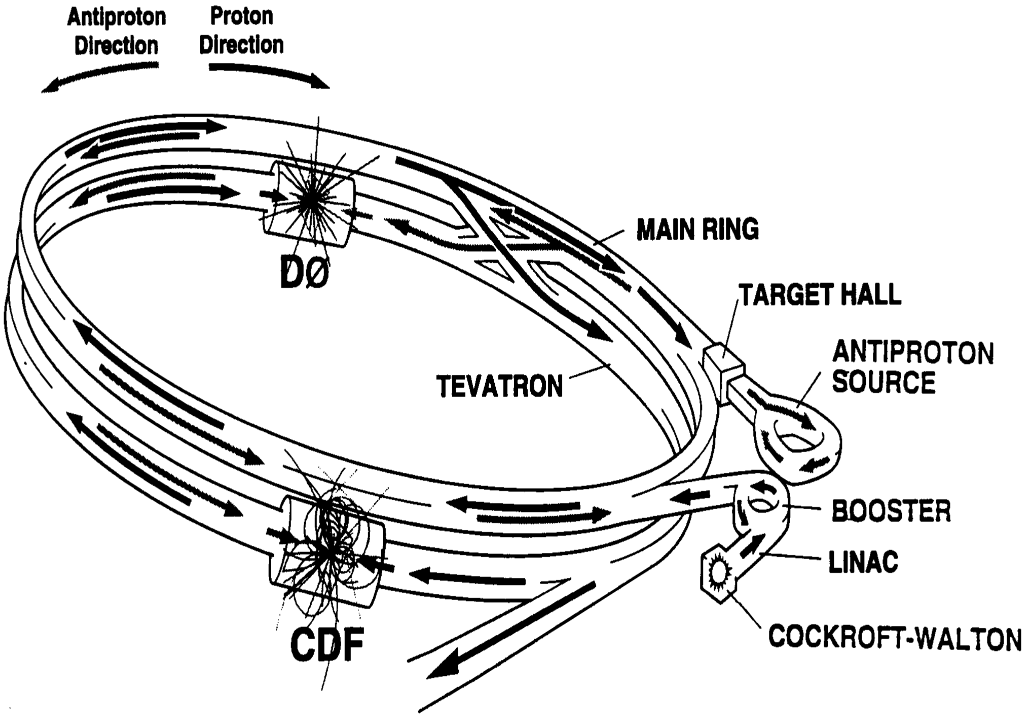

Figure 3.1: The Tevatron accelerator schematic layout.

The antiprotons created in these collisions have wide angular divergence and broad energy spectrum. They are initially focused with a lithium magnetic lens and injected into the first of two antiproton storage rings, the Debuncher. In this ring the antiproton energies are equalized, and the particles are formed into a compact beam (this process is known as *cooling*). Two processes are used to form such a mono-energetic antiproton beam: the debunching, and stochastic cooling. The former uses computer controlled radio-frequency pulses to smooth the antiproton store into a continuous ring where all particles have approximately the same momentum. The latter squeezes this ring in the transverse plane by using beam sensors which transmit information about the beam profile to kicker electrodes downstream. The electrodes introduce corrective magnetic fields which on average kick the antiprotons deviating from the beam center back into the beam. The cooling processes run continuously and prepare a monochromatic squeezed antiproton beam with $\sim 2 \cdot 10^6$ antiprotons for the second antiproton storage ring, or Accumulator. In the Accumulator the antiprotons are further cooled and their density is increased. When about $4 \cdot 10^{11}$ antiprotons are stored in the Accumulator (it typically takes 8 to 12 hours), they are transferred back into the Main Ring, accelerated, and injected into the Tevatron ring in the direction opposite to that of the proton beam.

The Tevatron ring uses superconducting magnets operating at liquid helium temperature (4 K) and producing a bending magnetic field of $\sim$ 4 T which allows for higher energy protons and antiprotons. When the filling of the Tevatron ring with both p and $\bar{p}$ is completed, the particles are formed into six proton and six antiproton bunches with about 10^{11} and $5 \cdot 10^{10}$ particles respectively per bunch, and accelerated to the maximum energy (0.9 TeV currently). After reaching the final energy the beams contain considerable halos, which are scraped with a metal plate collimator, before the CDF and DØ detectors start to collect physics data. The beams are held apart in the accelerator except at the two beam crossing points BØ (CDF) and DØ. The typical lifetime of the Tevatron beams, determined by beam scattering on the residual gasses in the Tevatron vacuum pipe, is about 12 – 18 hours. During this time new antiprotons are stored into the Accumulator which allows for a continuous operation of the Tevatron. The downtime between two subsequent Tevatron stores is about 2 hours.

The maximum luminosity achieved in run Ia was $\sim 9 \cdot 10^{30}$ cm^{-2}s^{-1}.

3.1.3 The Tevatron Future

Currently, the Tevatron is in the middle of run Ib which started in 1994 and will continue till the end of 1995. The luminosity of the Tevatron was increased since run Ia and the highest luminosity achieved to date in the current run is $1.2 \cdot 10^{31}$ cm^{-2}s^{-1}. It is expected that the accelerator will deliver about 100 pb^{-1} of physics data per experiment by the end of run Ib, thus increasing the statistics collected in run Ia by a factor of ~ 5.

The near future of the Tevatron is based on the Main Injector upgrade [55]. The Main Injector which will act as a booster to the Tevatron, will be located in a separate tunnel about half of the size of the Main Ring. This intermediate ring will allow luminosity of $\sim 10^{32}$ cm^{-2}s^{-1} in run II which is expected to take place in 1998 with upgraded CDF and DØ detectors. The Main Injector will also make it possible to run the collider and the fixed target programs simultaneously.

The more distant future of Fermilab is not clear yet. There are several proposals for further upgrade of the accelerator complex. One is the Super-Luminous Tevatron, which will operate at $\sqrt{s} = 2$ TeV with the instantaneous luminosity of $> 10^{33}$ cm^{-2}s^{-1} [56]. Another possible scenario is a DiTeV machine with new superconducting magnets which will be able to handle 2 TeV beams [56]. However, it is clear that further upgrades will not take place before the 21st century.

3.2 The DØ Detector

This section contains a brief description of the multipurpose DØ detector and some more details on the different subdetectors used for the analysis described in this Dissertation. A more thorough description of the DØ detector can be found in Ref. [57].

3.2.1 Overview

The DØ detector is a general purpose 4π particle detector dedicated for extensive studies of the high-p_T physics in $p\bar{p}$ annihilations at the Fermilab Tevatron collider (see sec. 3.1 for brief accelerator description). It was designed with an emphasis on superior calorimetry and muon identification, with less attention payed to the identification of the charged particles within jets. For these purposes, the design efforts were focused on building a compact and hermetic calorimeter with excellent hadronic and electromagnetic energy resolution. The calorimeter based on the use of uranium as a passive material, and liquid argon as the readout medium, is the heart of the DØ detector. In the tradition of the UA2 detector, DØ does not have a central magnetic field, thus

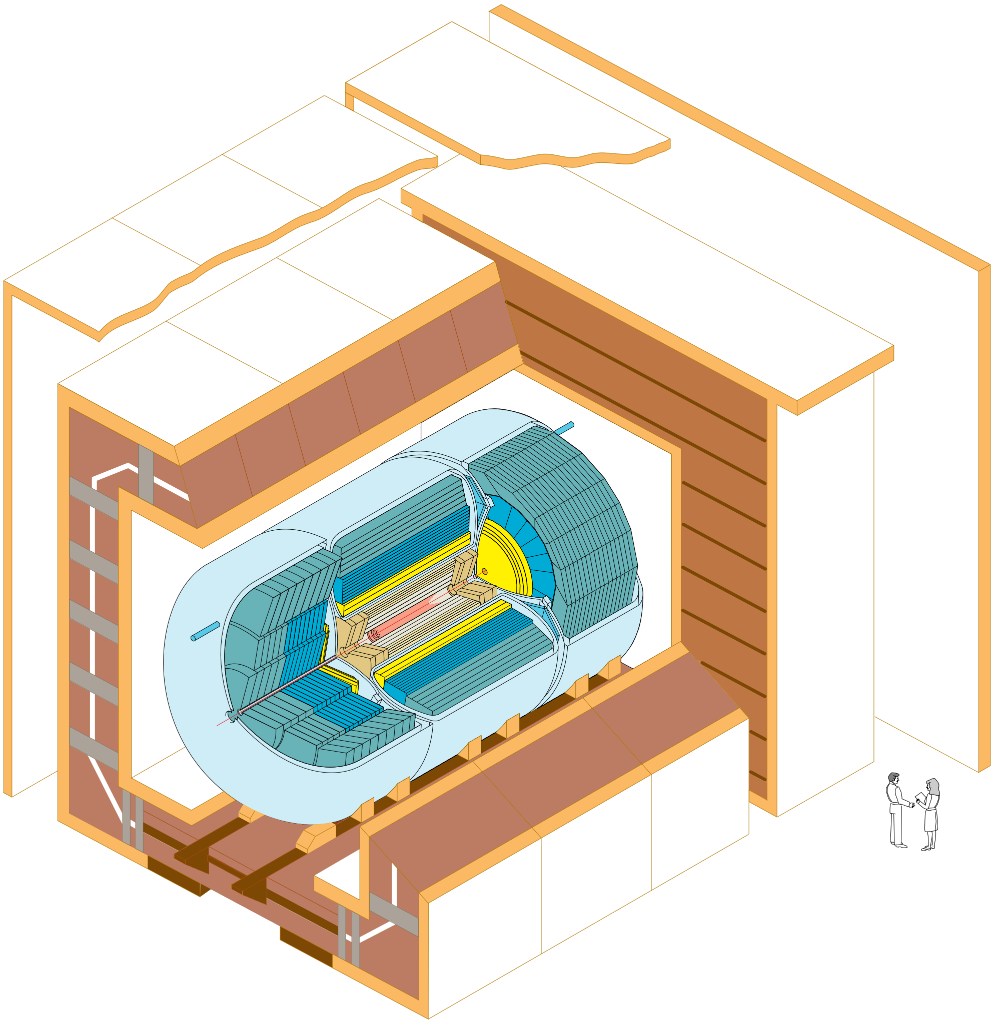

Figure 3.2: The DØ detector.

making the calorimeter extremely compact, and allowing for a full coverage muon system.

This philosophy made it possible to build DØ as a second generation detector complementary to the conventional warm-calorimetry CDF detector [58], operating at the same accelerator. Even without superior tracking, as CDF has, the DØ detector is capable of studying a wide variety of high energy phe-

Figure 3.3: The DØ Collaboration.

nomena, such as high precision electroweak physics, top-quark search, heavy quark physics, perturbative QCD, and new physics.

An isometric view of the DØ detector is shown in Fig. 3.2. Besides the liquid argon calorimeter, it consists of the other two main parts: the central tracking (located inside the calorimeter) and the three-layer muon tracking system with an iron toroidal magnet (surrounding the calorimeter).

The DØ detector is approximately 13 m high $\times$ 11 m wide $\times$ 17 m long with a total weight of about 5500 tons. The large dimensions and the weight are primarily due to the muon system. The detector was built and put into operation at a cost of thousands of man-years of labor (accomplished by engineers, technicians, and physicists) and 75 million dollars. As of today, the DØ Collaboration unites about 450 people of 44 scientific organizations located in 10 countries around the world (major participants are shown in Fig. 3.3).

The DØ Collaboration was organized in 1983 with Paul Grannis as its first spokesman. The full DØ proposal [59] was presented to the Physics Advisory Committee (PAC) of Fermilab in November, 1983. Detailed design and assembling of the detector took place in 1985 – 1992. The cosmic ray commissioning run was held in February – May, 1991. On February 14, 1992 the DØ detector was rolled into the collision hall, and on May 12, 1992 the first $p\bar{p}$ events were recorded on tape. At present, the detector is in the middle of its second physics run (run Ib). The spokesman duties are currently shared between Paul Grannis and Hugh Montgomery.

The DØ detector was built according to general principles of particle detection at high-energy hadron colliders (see, e.g. [60]). The tracking chambers are located as close as possible to the interaction point, prior to the massive calorimeter and muon system. The tracking detector is surrounded by the electromagnetic calorimeter layers, followed by a thick hadron calorimeter. The only particles which escape the calorimeter are muons (measured in the muon system) and neutrinos or other possible weakly interacting long-lived particles (detected by the energy imbalance in the detector). The calorimeter covers the pseudorapidity range $|\eta| < 4.5$ (see below for a definition of the pseudorapidity η), making the DØ detector almost hermetic. The only way energy can escape the detector is in the very forward region, through the beam-pipe traversing the center of the detector.

The azimuthal symmetry of the detector is violated by the Main Ring of the accelerator passing through the outer coarse hadronic layer of the calorimeter (see sec. 3.3) at a height of 89.2″ above the Tevatron ring (see sec. 3.1), the rectangular design of the muon system chambers, and the absence of one layer of the muon detectors in the area right underneath the calorimeter, occupied by mechanical support structures.

The DØ detector uses a reference frame defined by the Central Drift Chamber (CDC, see sec. 3.4.3). It has a right-handed coordinate system with z-axis along the direction of the proton beam and with a vertical y-axis. The polar coordinate system, used for definition of many physics parameters, has azimuthal angle (ϕ) defined so that $\phi = \pi/2$ points along y direction, and polar angle (θ) measured relative to the z-axis ($\theta = 0$ corresponds to the z-axis direction). For ultrarelativistic particles it is more convenient to use an approximate Lorentz invariant, pseudorapidity (η), instead of the polar angle. The pseudorapidity is defined as

$$\eta \equiv -\log\left[\tan\frac{\theta}{2}\right] = \tanh^{-1}(\cos\theta). \tag{3.1}$$

The positions of the other subdetectors relative to the CDC were surveyed by precise geodesic measurements and finely adjusted by matching tracks reconstructed in different tracking subdetectors and shower centers in the calorimeter [61].

The following sections discuss the details of different subsystems of the DØ detector.

3.3 Calorimeter

Being the centerpiece of the DØ detector, the liquid argon calorimeter is used not only for energy measurements, but as a source of additional information necessary for identification of muons, electrons, photons, and jets, as well as for missing transverse energy ($\not{E}_T$) measurements. Moreover, since the DØ detector does not have a central magnetic field, the calorimeter is the only source for determining the energy scale precisely.

3.3.1 Calorimeter Concept

Most modern high energy physics calorimeters use the *sampling* principle for energy measurements. A sampling calorimeter consists of a multilayer "sandwich" made of slices of a dense material with high atomic number (in which electromagnetic and hadron shower are developed), interleaved with slices of an active media (usually a scintillator or an ionization medium) which measure fractional energy depositions, or *sampling fractions*. These fractions, in general, are proportional to the incident particle energy.

The primary particle can interact with the calorimeter material via electromagnetic or strong interactions. The products of the interactions are known as electromagnetic or hadronic showers. The features of these two types of showers are quite different, and the calorimeter is typically subdivided into two parts — the inner one for the electromagnetic shower detection, and the outer one for the hadronic shower measurements. Since the nuclear interaction length (λ) in most heavy materials is much larger than the radiation length

(X_0), even a thick ($\gg X_0$) electromagnetic part typically contains only a fraction of λ, and therefore the electromagnetic calorimeter is rather transparent to hadrons. On the other hand, the thickness of the electromagnetic calorimeter ($\approx 20\ X_0$ in the DØ case) in most of the cases is sufficient to absorb the electromagnetic shower energy, so the hadronic and electromagnetic calorimeters work relatively independent of each other for the single-particle showers.

There are many important rules which must be satisfied for optimizing the calorimeter characteristics, such as energy resolution. For instance, the best hadronic energy resolution can be achieved with the so-called compensating calorimeters [62], which have equal response to the electromagnetic and hadronic showers of the same energy. The reason for this is large fluctuations of the electromagnetic component (due to the π^0's, η's production with further radiative decays) in hadronic showers. If the calorimeter has different response for electrons and pions, these fluctuations translate into the statistical uncertainty in the energy deposited in the readout medium, and, therefore, into the resolution. For most of the sampling calorimeters electron response is higher than hadronic [63].

To equalize the electromagnetic and hadronic responses, the DØ calorimeter uses depleted uranium as a passive material (absorber) for the electromagnetic and inner hadronic layers. The idea to use uranium-238 in the hadronic calorimeters is rather old [64]. The original motivation was that due to the nuclear break-ups and neutron-induced fission in a radioactive uranium, part of the normally invisible energy converts into a detectable one, which increases the hadronic response. However, it turned out that in reality the compensation is mostly due to a decrease of electron response in a high-Z absorber material [63]. In addition to accounting for the nearly identical hadronic and electromagnetic response, the uranium, being very dense, makes the calorimeter extremely compact. Stainless steel and copper are used as absorbers in the outer hadronic layers. Liquid argon was chosen as an active (ionization) medium for all DØ calorimeters. This choice gives a unit gain and radiation hardness of the calorimeter at the cost of low operating temperature (86K) which requires a cryostat and a cryogenic system.

A detailed description of the calorimeter design principles and applications of liquid argon and other calorimeters in high energy physics can be found in Refs. [51, 62, 63, 65].

3.3.2 Readout Design

DØ calorimeters use absorber plates of different thickness ($3 - 46.3$ mm) made of different materials. However, usage of uniform readout structures made it easy to use the same cell design for all calorimeters. A schematic view of the unit cell is shown in Fig. 3.4. The gap between adjacent absorber plates is filled with liquid argon. The electron-ion pairs (created in the liquid argon by charged particles from electromagnetic or hadronic showers) are collected by the electrodes in presence of a strong electric field. Metal absorbers are used as ground electrodes (cathodes), and the readout boards at $+2.0$ to 2.5 kV, located in the center of the gaps, serve as anodes. Each board in most of the modules is a sandwich of copper readout pads between two 0.5 mm plates of

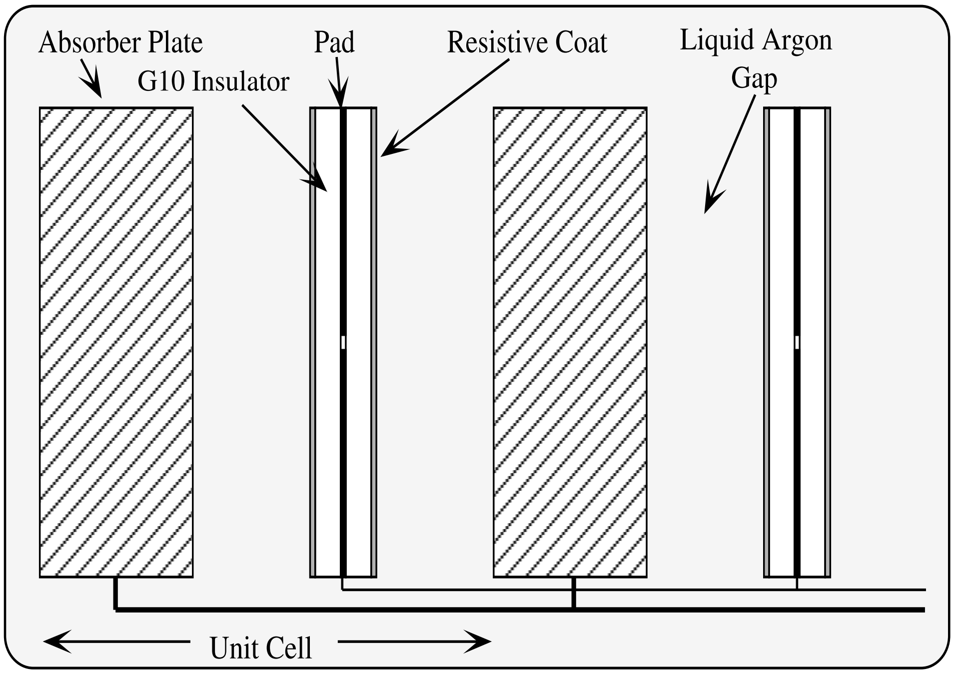

Figure 3.4: Schematic view of the liquid argon calorimeter unit cell.

G10 plastic covered with a resistive epoxy coating. High voltage is applied to the entire resistive coat, and the charge collection in this coat induces a charge on the copper readout pads via capacitative coupling. The electromagnetic and small-angle hadronic modules in the end calorimeter (see sec. 3.3.5) have multilayer printed circuit readout boards. The gap between absorber plate and readout pad in most of the cases is 2.3 mm, which corresponds to a typical electric field of 9 kV/cm and an average electron drift time of 450 ns. The gap thickness was chosen to be large enough to observe minimum ionizing particle signals in the calorimeters, which is an important requirement for muon identification (see sec. 4.1.3).

There is no charge multiplication in the liquid argon, so the signals from the readout pads can be small. To detect them, several pads are ganged together in depth to form a readout cell (see sec. 3.3.3). Charge-sensitive preamplifiers mounted on the calorimeter cryostat integrate the ganged signals and pass them to the base-line subtraction modules located on the detector platform. They split the signal into two paths — the one used by the fast Level 1 trigger (see sec. 3.6.2), and the main data path where signals are properly shaped, digitized in 12-bit analog-to-digital converters (ADC's) and fed into the data acquisition system (see sec. 3.6.3). Fast Level 1 trigger electronics combine the readout cells into $\Delta\eta \times \Delta\phi = 0.2 \times 0.2$ trigger towers and provide information about the energy deposition in each of the towers (within 2.2 μs from the beam-crossing time).

3.3.3 Calorimeter Geometry

The DØ calorimeter consists of the Central Calorimeter (CC) and two mirror-image End Calorimeters (EC) described in details in separate sections. Each calorimeter is located in its own cryostat and has a modular structure with the modules of three distinct classes: electromagnetic (EM), fine hadronic (FH), and coarse hadronic (CH). Such a design is determined by the differences in the longitudinal development of the electromagnetic and hadronic showers. An isometric view of the DØ calorimeter is shown in Fig. 3.5.

The transverse sizes of the readout cells in different modules are chosen to be of the same order as the diameters of the corresponding showers (≈ 2 cm for electromagnetic and ≈ 10 cm for hadronic). Physical cells are ganged together

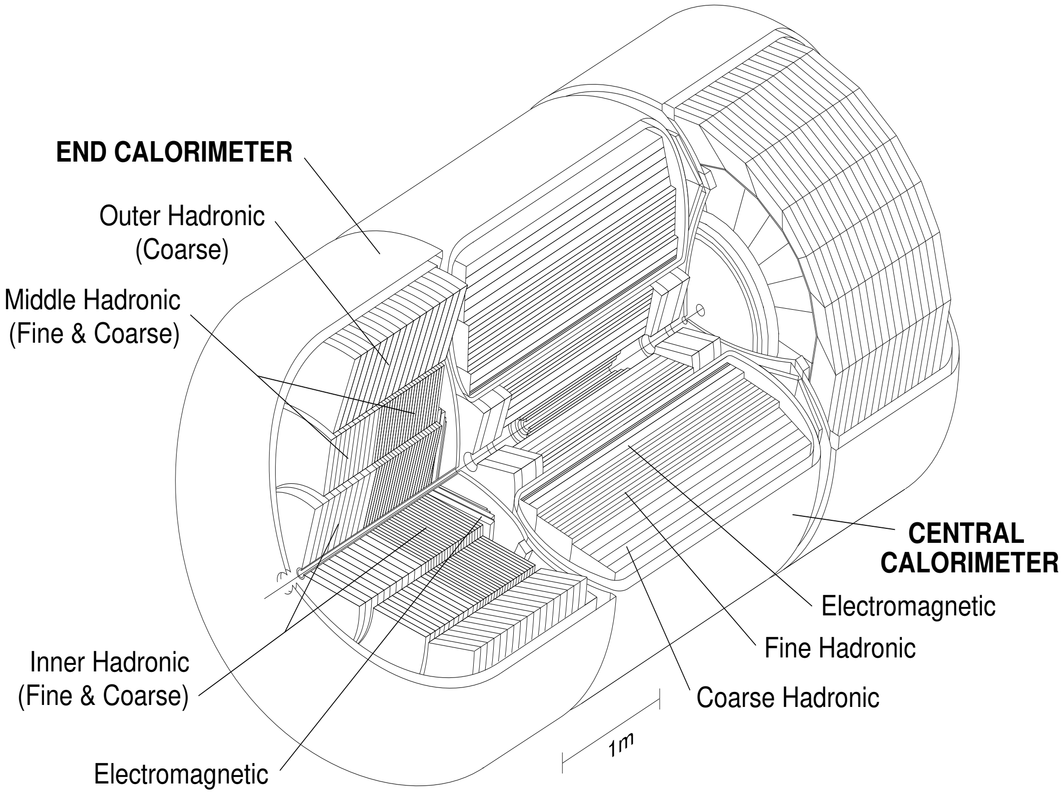

Figure 3.5: DØ liquid argon calorimeter.

in depth to form a readout cell using a pseudo-projective geometry, as shown in Fig. 3.6. The term *pseudo-projective* refers to the fact that the centers of the cells of increasing shower depth point to the interaction vertex, whereas the cell boundaries are perpendicular to the absorber plates [57]. Typically, the transverse segmentation of the readout towers is $\Delta\eta \times \Delta\phi = 0.1 \times 0.1$.

An important feature of the DØ calorimeter is the fine longitudinal segmentation which is essential for distinguishing between π^0's and electrons (see sec. 4.1.1), as well as for the jet reconstruction. The EM modules consist of four separate layers, EM1 to EM4. Each layer uses 3 mm or 4 mm thick de-

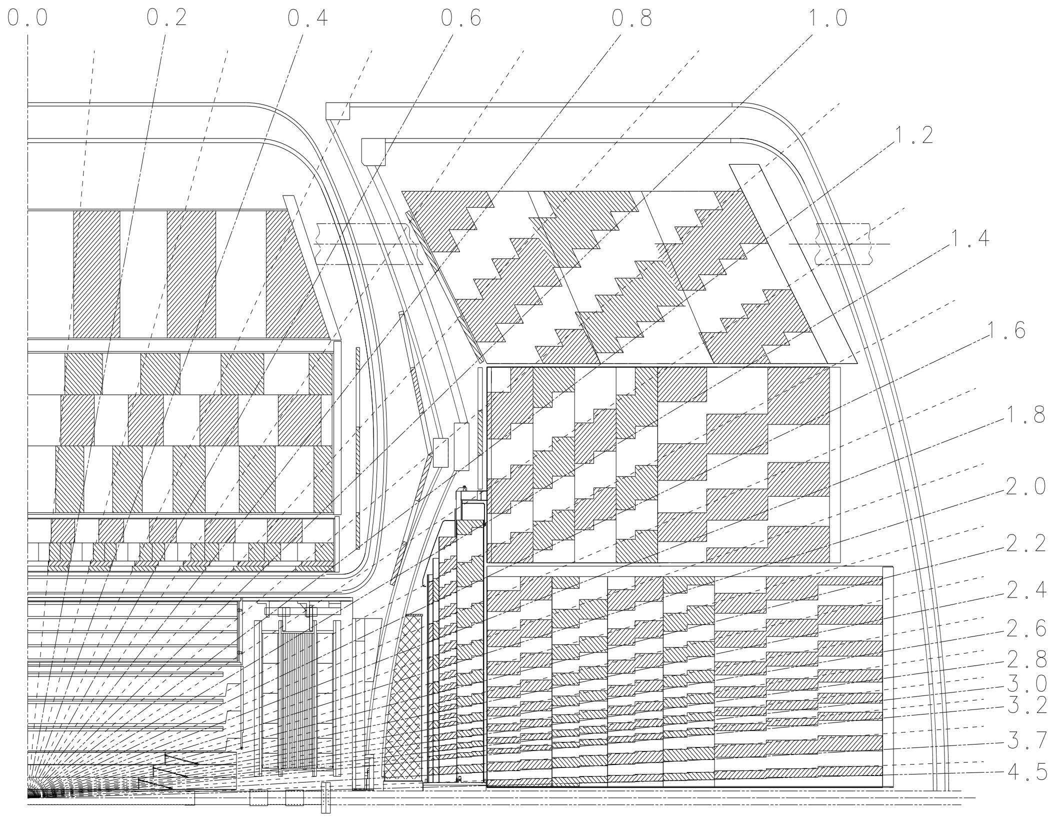

Figure 3.6: Pseudo-projective geometry of the readout calorimeter cells.

pleted uranium plates as an absorber. The FH modules consist of three or four layers with 6 mm depleted uranium (doped with 1.7% niobium) plates as an absorber. The outer CH module has only one layer with thick (46.5 mm) stainless steel or copper absorber. The longitudinal arrangement of the calorimeter towers as a function of η is shown in Fig. 3.7. The fine hadronic layers measure the energy and position of penetrating hadrons, such as charged pions. The coarse hadronic layer protects against punchthrough and leakage of hadronic showers due to large fluctuations in the longitudinal shower development. The total thickness of the calorimeter is $7 - 10\ \lambda$.

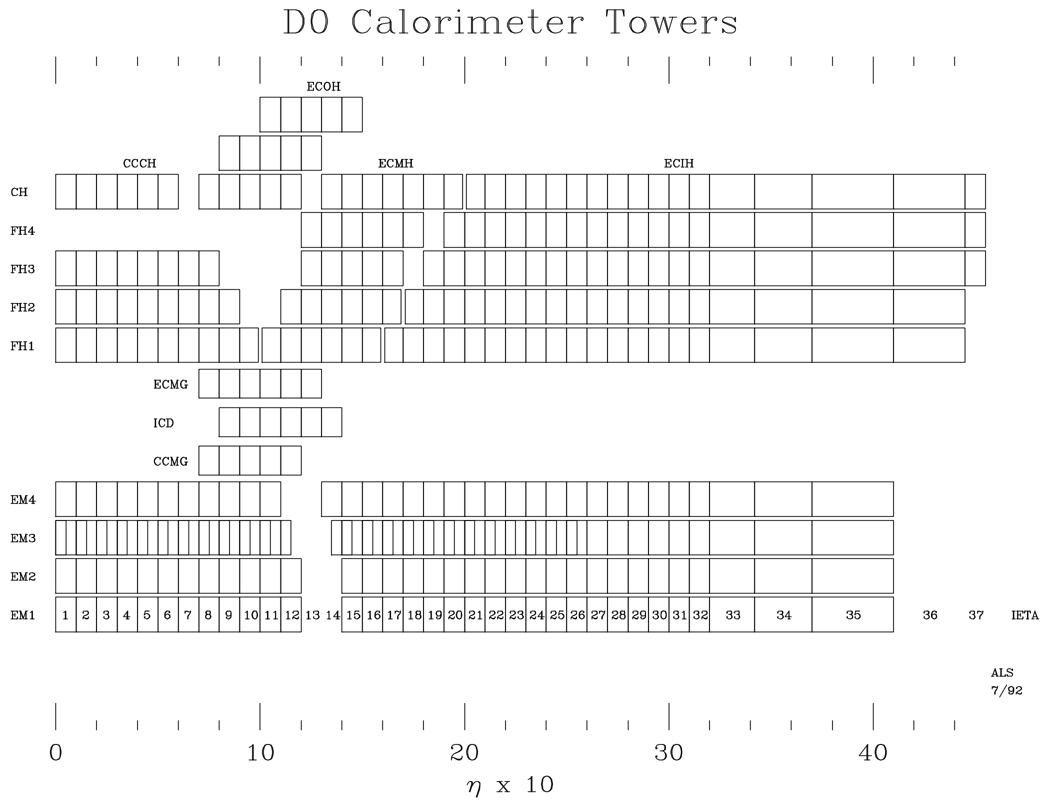

Figure 3.7: Longitudinal arrangement of the readout calorimeter cells.

3.3.4 Central Calorimeter

The Central Calorimeter (CC) [57] (see Fig. 3.5) consists of the inner ring of 32 CCEM modules and two hadronic calorimeter rings with 16 CCFH and 16 CCCH modules, respectively. The module boundaries in the three rings are shifted one relative to the other, so that no projective ray encounters more than one intermodule gap. The CC has a length of 2.6 m, and covers the pseudorapidity interval $|\eta| < 1.2$. The total weight of the CC modules and the support structure is 305 tons, with an additional 26 tons contributed by liquid argon [57].

Module type	CCEM	CCFH	CCCH
Pseudorapidity coverage	± 1.2	± 1.0	± 0.6
Number of modules	32	16	16
Absorber	U	UNb	Cu
Absorber thickness (mm)	3	6	46.5
Argon gap (mm)	2.3	2.3	2.3
Readout cells per module	21	50	9
Longitudinal depth ($\eta = 0$)	$20.5\ X_0 = 0.76\ \lambda$	$3.2\ \lambda$	$3.2\ \lambda$
Number of readout layers	4	3	1
Cells per readout layer	2/2/7/10	20/16/14	9
Depth per readout layer	$2.0/2.0/6.8/9.8\ X_0$	$1.3/1.0/0.9\lambda$	3.2λ
Sampling fraction (%)	11.79	6.79	1.45
Segmentation ($\Delta\phi \times \Delta\eta$)	EM1,2,4: 0.1×0.1 EM3: 0.05×0.05	0.1×0.1	0.1×0.1
Total number of channels	10,368	3,000	1,224

Table 3.1: Central Calorimeter vital statistics.

The first two EM layers with a thickness of $\approx 2\ X_0$ each and a transverse segmentation of 0.1×0.1 are used to measure the longitudinal profile of an electromagnetic shower near its origin. This profile differs statistically for the showers induced by electron/photon and π^0 decaying into a pair of spatially close photons. The third layer, located at the shower maximum has finer transverse segmentation of 0.05×0.05 in (η, ϕ), which allows for more accurate measurement of shower centroid positions. The fourth layer completes the total EM coverage of $\approx 21\ X_0$ or $\sim 0.8\ \lambda$.

Major characteristics of the CC are given in Table 3.1 [57, 66, 67].

3.3.5 End Calorimeters

Each of the two mirror-image End Calorimeters (EC) [57, 68] (see Fig. 3.5) also has a modular structure. It consists of an electromagnetic module (ECEM), an inner fine hadronic module (IFH), an inner coarse hadronic module (ICH), and two concentric rings of middle fine hadronic/middle coarse hadronic (MCF/MCH), and outer coarse hadronic (OCH) modules (16 modules in each ring). The ECEM and FH calorimeters have an uranium absorber[1]; stainless steel (SS) is used in the coarse calorimeters.

The EC primarily covers the pseudorapidity interval $1.1 < |\eta| < 4.5$. For pseudorapidities of $1.1 < |\eta| < 1.5$ particles traverse little or no EM layers, but do encounter the OCH or MFH modules (see Fig. 3.6). The reconstruction of the electromagnetic energy in this region is unreliable (see sec. 3.3.6). In the region $1.5 < |\eta| < 2.0$, particles pass through the ECEM, IFH, MFH, and MCH modules. In the very forward region, $2.0 < |\eta| < 4.5$, particles pass only through ECEM, IFH, and ICH modules. The OCH modules of the EC extend the rapidity coverage down to $|\eta|$ values of 0.8, which is the transition region between the CC and EC (see discussion in sec. 3.3.6).

The segmentation of the most of the EC readout cells is 0.1×0.1 in (η, ϕ), except for the segmentation of the EM3 layer of ECEM which is twice as fine (as in the CCEM case), and increasing transverse cell size in the very forward region ($|\eta| > 3.2$) which reaches the maximum of 0.4×0.4 in (η, ϕ) for cells in

[1]Some of the ECEM cells use the stainless steel absorber plates to achieve more uniform sampling fraction [68].

Module type	ECEM	IFH	ICH	MFH	MCH	OCH
$\|\eta\|_{min}$	1.3	1.6	2.0	1.0	1.3	0.7
$\|\eta\|_{max}$	4.1	4.5	4.5	1.7	1.9	1.4
N of modules	1	1	1	16	16	16
Absorber	U/SS	UNb	SS	UNb	SS	SS
Abs. thick. (mm)	4	6	46.5	6	46.5	46.5
Argon gap (mm)	2.3	2.1	2.1	2.2	2.2	2.2
Cells/module	18	64	14	60	12	24
Longitudinal depth	20.1 X_0 0.95λ	4.4λ	4.1λ	3.6λ	4.4λ	4.4λ
N of readout layers	4	4	1	4	1	3
Cells/readout layer	2/2/6/8	16	14	15	12	8
Sampling (%)	≈ 8	5.7	1.5	6.7	1.6	1.6
$\Delta\phi$ segmentation	0.1/0.05	0.1–0.4	0.1–0.4	0.1	0.1	0.1
$\Delta\eta$ segmentation	0.1/0.05	0.1–0.4	0.1–0.4	0.1	0.1	0.1
N of channels	7,488	4,288	928	1,472	384 + 64 + 896	

Table 3.2: End Calorimeter vital statistics.

the ECEM, IFH, and ICH at $|\eta| \approx 3.7$ (see Fig. 3.7). The EM1 layer of the ECEM is only 0.3 X_0 thick, since the cryostat wall brings the total absorber thickness of the first section up to ≈ 2.0 X_0.

The overall weight of the EC calorimeter is 238 tons. Many other parameters of the End Calorimeter are listed in Table 3.2 [57, 66, 67, 68].

3.3.6 ICD and Massless Gap Detector

The pseudorapidity interval $0.8 < |\eta| < 1.5$ is a transition region between the Central and End Calorimeters (see Fig. 3.6). It contains a large amount of uninstrumented material, like cryostat walls, module endplates, etc. The amount of energy deposited in this material is not detected. For instance, the electromagnetic energy is not reconstructed correctly in the pseudorapidity range $1.1 < |\eta| < 1.5$. To correct for the energy loss in the transition region, DØ implemented two separate devices, the InterCryostat Detector (ICD) [57], and the Massless Gaps (MG) [57].

The ICD is an array of the scintillating modules mounted on the surface of the EC cryostat between the CC and EC (see Fig. 3.6). The ICD of each EC consists of 384 scintillator tiles of size 0.1×0.1 in (η, ϕ), which match the pseudo-projective towers in the calorimeter. The ICD readout is based on the phototubes [57].

In addition to the ICD, there are three rings of the MG detectors mounted inside the cryostats on the surfaces of the CCFH, MFH, and OCH modules. The MG detector consists of two readout boards surrounded by three liquid argon gaps. There are no absorber plates in the MG. The size of the MG cells is 0.1×0.1 in (η, ϕ) [57]. There are 320 readout channels in the CCFH ring and total of 192 channels in the MFH and OCH rings.

Together, the ICD and MG provide a reasonable approximation to the standard DØ sampling of the electromagnetic showers.

3.3.7 Calibration and Energy Resolution

As was mentioned above, the calorimeter is the only source of a precise energy scale in the DØ detector. Therefore, a precise calorimeter calibration is very important. Approximate calibration constants were obtained using the electron and pion test beams [71, 72]. They were further adjusted *in situ* for the electromagnetic calorimeter by comparing the positions of the peaks in the measured dielectron mass spectrum with the world average values of Z, J/Ψ, and π^0 masses [73, 74]. It was shown [73, 74] that the nonlinearity of the energy scale in the calorimeter is $< 0.5\%$.

The energy resolution of a sampling calorimeter is determined by the fluctuation of the number of ion pairs produced by a shower in sampling media. Several sources contribute to these fluctuations (see [51, 62]): sampling fluctuations, or fluctuations in the actual energy deposited in active media, leakage of energy out of the calorimeter, fluctuations in the calorimeter response due to changing operating conditions (such as the temperature and purity of the liquid argon, high voltage, etc.), and noise in the active layers (due to natural radioactivity of the uranium, readout electronics thermal noise, etc.).

The resolution of the sampling calorimeter can be parameterized in the following form:

$$\left(\frac{\sigma_E}{E}\right)^2 = C^2 + \frac{S^2}{E} + \frac{N^2}{E^2}, \tag{3.2}$$

where constants C, S, and N represent calibration errors, sampling fluctuations, and noise contributions, respectively. The noise term is usually negligible, except for very low energies [51].

The resolution for the DØ calorimeter was measured in the test beam for electrons and pions [57]:

$$\left(\frac{\sigma(E_{EM})}{E_{EM}}\right)^2 = (0.003 \pm 0.002)^2 + \frac{(0.157 \pm 0.005)^2}{E_{EM}\ [\mathrm{GeV}]}, \tag{3.3}$$

$$\left(\frac{\sigma(E_h)}{E_h}\right)^2 = (0.032 \pm 0.004)^2 + \frac{(0.41 \pm 0.04)^2}{E_h\ [\mathrm{GeV}]}. \tag{3.4}$$

The noise term is indeed small (typical noise is $\sim$ 100 MeV per readout tower).

Complete compensation in EM and FH layers has not been achieved. The ratio of the e and π responses in these layers varies from 1.11 at 10 GeV to 1.04 at 150 GeV [50].

The hadronic energy resolution of the calorimeter determines the calorimeter missing transverse energy ($\not{E}_T^{cal}$) resolution (i.e. the resolution in the $\not{E}_T$ calculated based on the calorimeter information only). It was measured using dijet data as a function of scalar sum of the E_T of the event, S_T [69, 70]:

$$\begin{aligned} \sigma(\not{E}_T^{cal}) &= (1.89 \pm 0.05)\ \mathrm{GeV} + (6.7 \pm 0.7) \cdot 10^{-3} S_T + \\ & (9.9 \pm 2.1) \cdot 10^{-6} S_T^2/\mathrm{GeV}. \end{aligned} \tag{3.5}$$

3.4 Central Tracking

Tracking is a special issue, since the DØ detector does not have a central magnetic field. On one hand this simplifies track-finding algorithms and the detector design. However, on the other hand, the absence of a magnetic field does not allow for the reconstruction of particle momenta which, together with the calorimeter information, could aid a lot to particle identification.

Central tracking is very important in DØ, since it is the only way to distinguish between electrons and photons. Furthermore, track information, like

dE/dx, multiplicity of the tracks, etc., is essential for distinguishing between converted photons/pions and electrons. Central tracking is also used for identification of other types of particles (e.g. muons). Additionally, central tracks are used for reconstruction of the z-position of the primary interaction point and possible secondary vertices.

The tracking in DØ is done in the Central Detector (CD) which consists of four independent subdetectors (see Fig. 3.8). Closest to the beam, there is a Vertex chamber (VTX), followed by the Transition Radiation Detector (TRD), and Central Drift Chamber (CDC). Tracking in the forward region is done in two Forward Drift Chambers (FDC's). The whole CD is contained in the cylindrical space (r = 78 cm, $z = \pm 135$ cm) bounded by the calorimeter cryostats (see sec. 3.3).

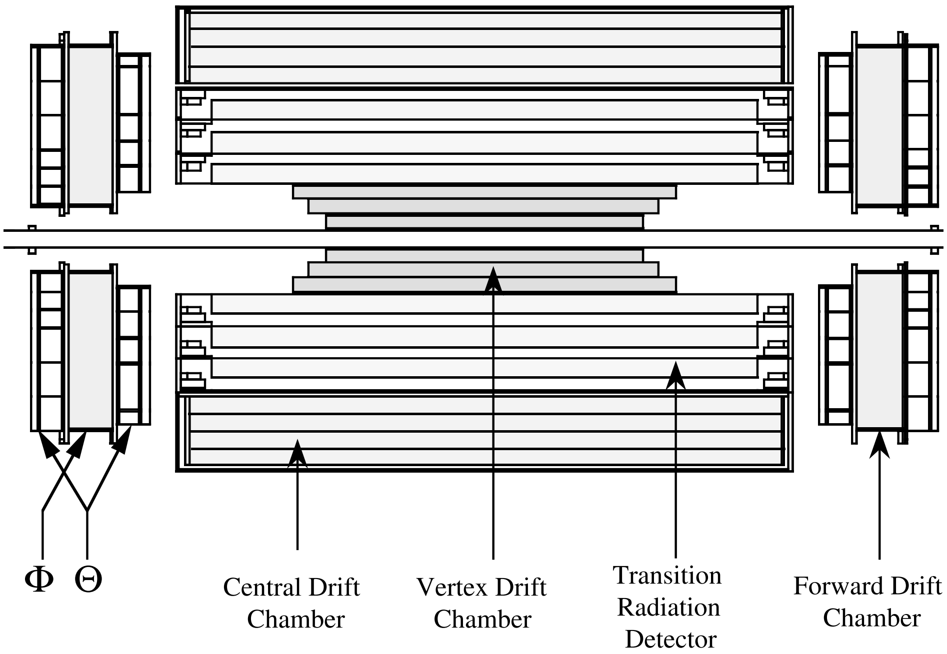

Figure 3.8: Central Detector layout.

All tracking detectors except the TRD are regular wire drift chambers (see Ref. [75] for details of the drift chamber operation). Both VTX and CDC have wires parallel to the beam for precise track measurement in the $r - \phi$ plane. The z coordinate is measured by a charge division method in the VTX and with the delay lines in the CDC. Each FDC has three sets of wire chambers: the middle one has radial wires and used for measuring ϕ information on the track; the two outer chambers have approximately axial wire planes. The outer chambers are rotated one relative to the other by $\pi/4$ (see sec. 3.4.4). The TRD also uses drift chambers for the detection of the X-rays of the transition radiation (see sec. 3.4.2).

The CD was designed to match the collider bunch-crossing interval of 3.5 μs, which allows for relatively long drift cells. The design was optimized to obtain a good spatial and two-track resolutions. Fast 8-bit flash analog-to-digital converters (FADC) [76] with ≈ 10 ns sampling time are used in the CD readout system for this purpose. With the typical drift velocity of $10 - 35$ μm/ns this corresponds to an effective detector granularity of $100 - 300$ μm with relatively small ($\approx 6,000$) total number of readout channels [57]. Before digitizing, the signals are amplified in Fujitsu MB43458 quad common base preamplifiers [77] mounted on the chamber surfaces, and further shaped by the shapers located in the DØ detector platform. The tracking electronics flow chart is shown in Fig. 3.9. The electronics is discussed in more detail in [57].

The following sections describe details of the CD subdetectors. Despite the fact that only the CDC and FDC information was primarily used in the

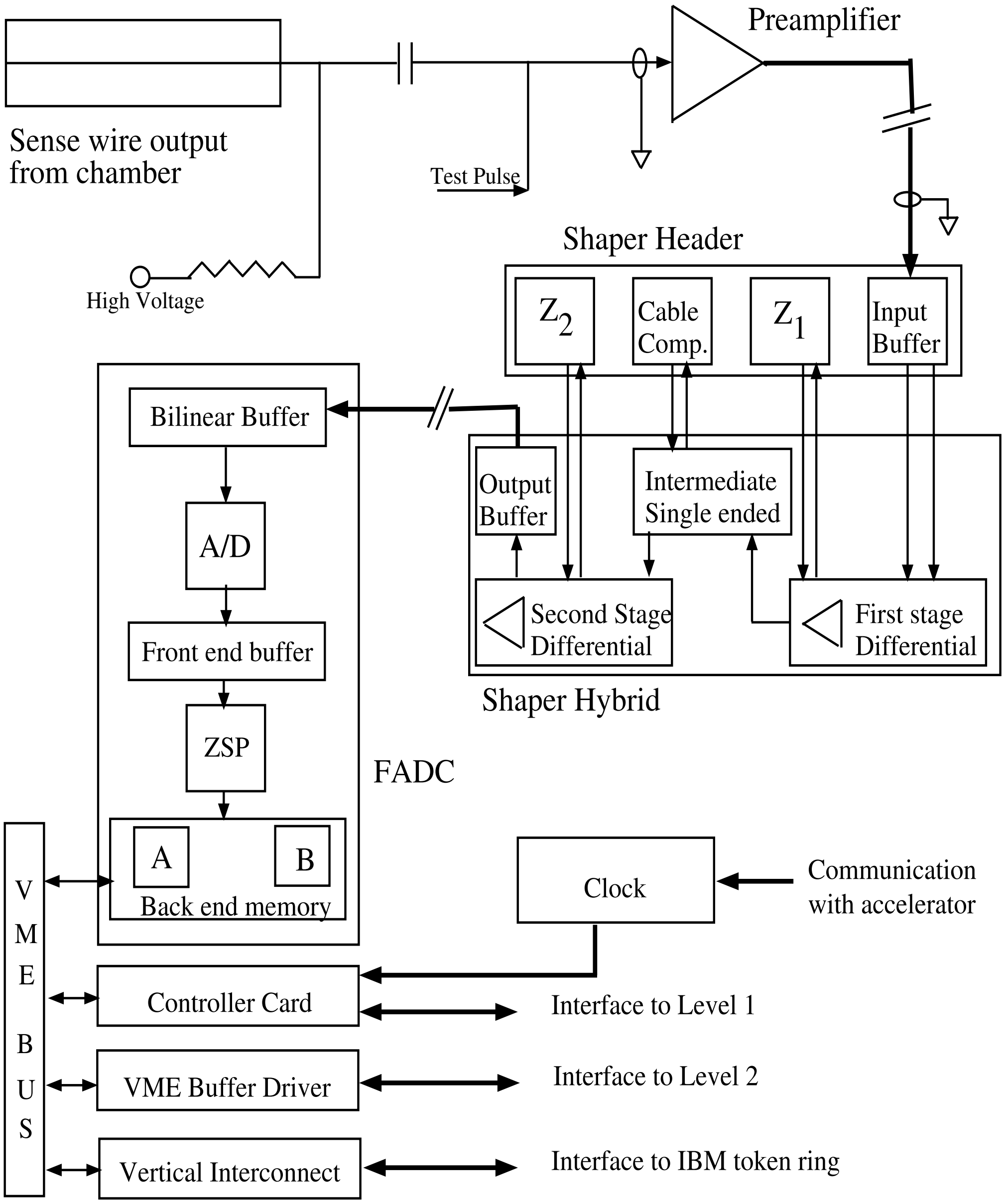

Figure 3.9: Schematics of the Central Detector electronics.

actual physics analysis described in this Dissertation, the details of the VTX and TRD chambers are also relevant to the extensions of this work, since we plan to utilize the information provided by these detectors for selecting $Z\gamma \rightarrow \nu\bar{\nu}\gamma$ events which are contaminated by a large $W \rightarrow e\bar{\nu}$ background (see sec. 4.4).

3.4.1 Vertex Chamber

The Vertex Chamber (VTX) [78] is the innermost tracking detector in DØ (see Fig. 3.8). Its inner radius (3.7 cm) is determined by the size of the beryllium beam pipe, and the outer active radius is 16.2 cm. It fully covers the pseudorapidity range of $|\eta| < 2.0$.

An original design goal of the VTX was to resolve secondary vertices from heavy quark decays and to complement the other tracking detectors in track parameter measurements. The VTX was designed to have the spatial resolution of $\sim$ 50 μm in $r - \phi$ plane. This requires an extremely precise placement of the sense wires ($\approx$ 25 μm, which is comparable with the diameter of the wire itself) and a drift time measurements with an accuracy of a few nanoseconds [60].

The chamber consists of three concentric layers of drift cells separated by a support structure of four carbon fiber tubes (see Fig. 3.10). The inner ring contains 16 drift cells; each outer ring has 32 cells. The $r - \phi$ coordinate in a cell is measured by 8 axial sense wires made of 25 μm NiCoTin alloy (38.3% Co, 19.3% Cr, 15.6% Ni, 13.3% Fe, and 11.4% Mo). Adjacent wires

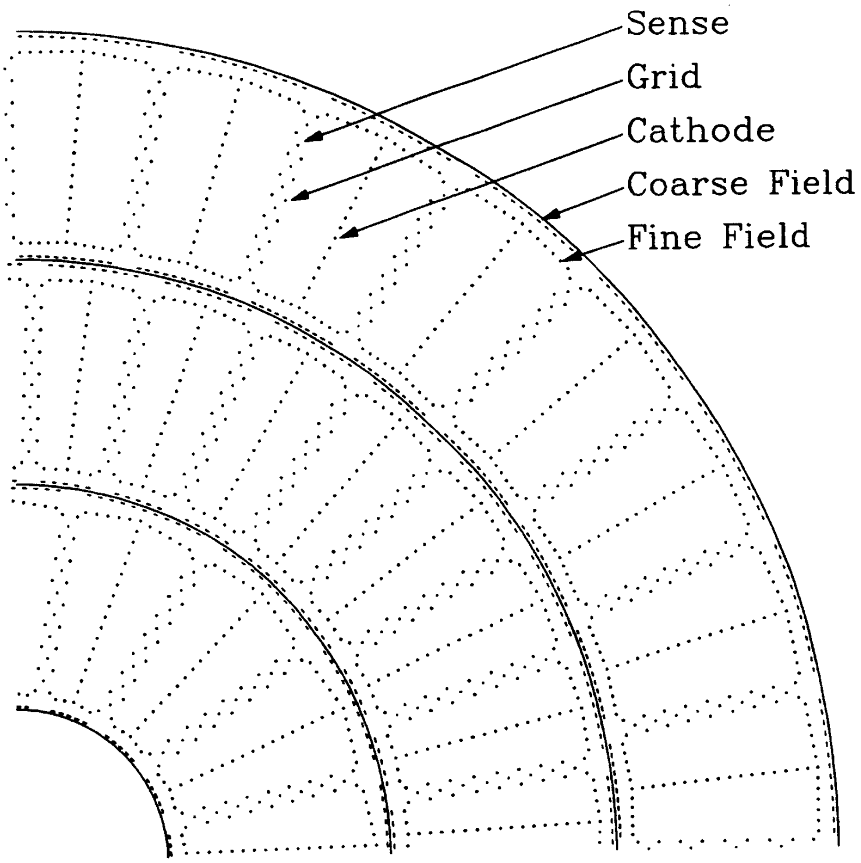

Figure 3.10: End view of a Vertex Chamber quadrant.

are staggered by ± 100 μm to resolve left-right ambiguities; the three layers are also shifted in ϕ relative to each other to further improve track reconstruction. Field and grid wires are made of 152 μm gold-plated aluminium. Coarse field shaping is provided by aluminium strips mounted on the support tubes. The wires are mounted on thin G10 plastic bulkheads with the tension supported by titanium rods (see Fig. 3.11) [57].

The z-coordinate in the VTX is reconstructed via the charge-division technique which is based on the difference in the signal amplitudes on both sides of the resistive sense wire [57].

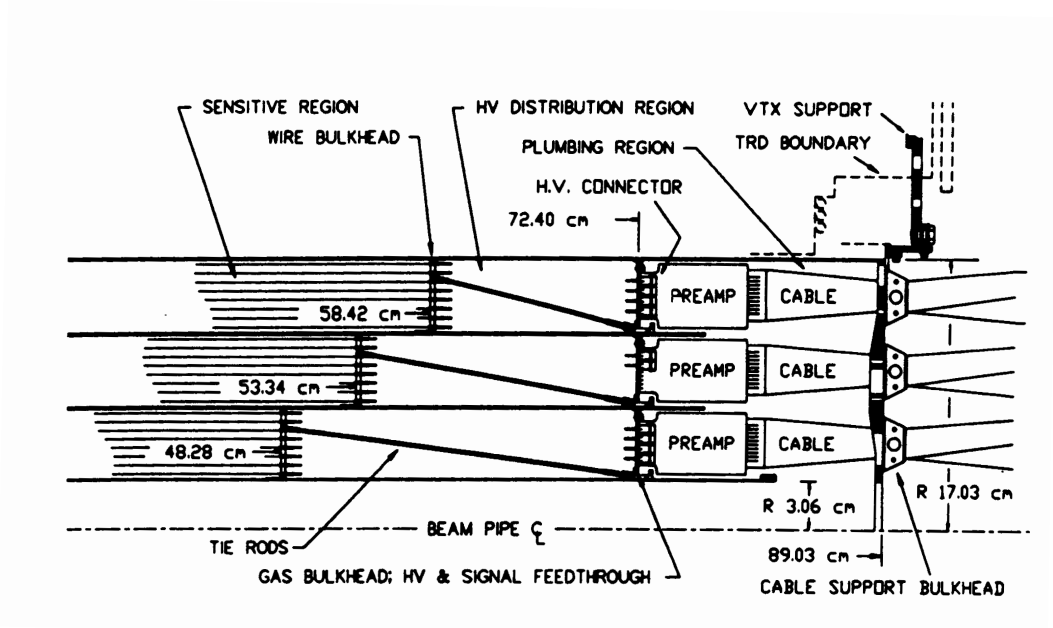

Figure 3.11: Endplate of the Vertex Chamber with wire and cable supporting structures.

The VTX uses a 95% CO_2/5% C_2H_6 gas mix with a small admixture of H_2O at the atmospheric pressure. This mix yields a relatively low drift velocity ($\approx$ 7 μm/ns), as required for high spatial resolution. The VTX resolution is typically 60 μm in $r - \phi$ and 1.5 cm in z directions [80].

For the real high-luminosity physical environment the track reconstruction in the VTX chamber has not been tuned well enough yet. Therefore, the VTX information is used for particle identification in the current analysis only for the cases when a reconstructed VTX track well matches a track in the CDC or FDC (which occurs only for $\approx$ 10% of CDC/FDC tracks). We, however, started to use the VTX hit information for improving the electron/photon separation for the $Z\gamma \to \nu\bar{\nu}\gamma$ event selection (see sec. 4.4).

The major parameters of the VTX chamber are listed in Table 3.3 [50, 57].

Parameter	Specification
Number of layers	3 (Layer0/Layer1/Layer2)
Radius [79] (R_{in}/R_{out})	Chamber: 3.7/16.2 cm Layer0: 3.73/6.9 cm Layer1: 8.40/11.60 cm Layer2: 13.00/16.23 cm
$\lvert\eta\rvert$-coverage [79] $(\lvert\eta_{in}\rvert/\lvert\eta_{out}\rvert)$	Chamber: 3.25/2.00 Layer0: 3.25/2.64 Layer1: 2.55/2.23 Layer2: 2.21/2.00
Length of active volume/layer	96.6/106.6/116.8 cm
Number of sense wires/cell	8
Number of sense wires	640
Radial wire interval	4.57 mm
Gas type	95% CO_2 + 5% ethane +0.5%H_2O
Gas pressure	1 atm
Sense wire potential	+2.5 kV
Nominal drift field	1.0 kV/cm
Average drift velocity	7.3 μm/ns
Gas gain	$4 \cdot 10^4$
Sense wire specifications	25 μm NiCoTin, 80 g tension
Field wire specifications	152 μm Au plated Al, 360 g tension
Spatial resolution	$r-\phi$: 60 μm; z: 1.5 cm

Table 3.3: Vertex Chamber specifications.

3.4.2 Transition Radiation Detector

The Transition Radiation Detector (TRD) [83] is located just outside the VTX (see Fig. 3.8). It is used exclusively as a source of an additional information for electron identification and separation of electrons from $\pi^0 \to 2\gamma$ decays or from prompt photons, converted outside the active TRD volume. The TRD is not used, however, in the analysis described in this work, because other particle identification criteria turned to be sufficient for the selection of rare $\ell^+\ell^-\gamma$ events (see sec. 4.1.1 and 4.1.2). It might be possible to use this detector for the $Z\gamma$ analysis in the future, particularly for selection of the $Z\gamma \to \nu\bar{\nu}\gamma$ events contaminated by a large $W \to e\bar{\nu}$ background (see sec. 4.4).

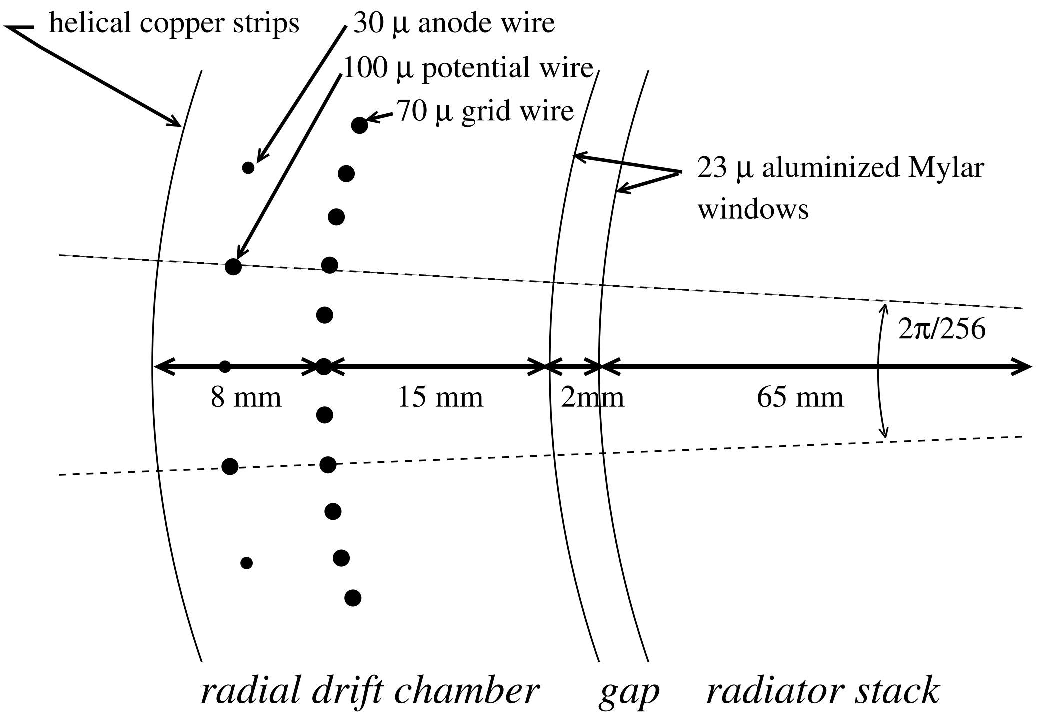

Figure 3.12: End view of a Transition Radiation Detector module.

The TRD detects the transition radiation of an ultrarelativistic charged particle crossing the boundary of two media with different dielectric properties [82]. For the DØ configuration this radiation is primarily emitted in form of X-rays with an energy peaking at 8 keV and mainly contained below 30 keV [57].

The TRD is made of three radial layers. Each layer consists of a radiator followed by a drift chamber for the X-ray detection. The radiator contains 393 layers of 18 μm thick polypropylene foils with a mean separation of 150 μm, in a volume filled with nitrogen gas. A large number of transitions (foil/gas) is essential, since the number of photons radiated in each transition is small.

The detection of the electrons produced by a photoelectric absorption of the X-rays, as well as by ionization induced by the relativistic charged particles passing through TRD, is done in a two-stage time-expansion drift chamber. The X-rays convert mainly in the first stage of the chamber filled by the Xe-based gas mix with low radiation length. The resulting electrons drift radially towards the sense wires in the second stage of the chamber, separated from the first one with a grounded wire grid (see Fig. 3.12). The sense wires measure the collected charge and the arrival time. The z-coordinate is determined by a set of helical copper pads mounted on the outer wall of the chamber.

The drift chambers are subdivided in sectors in ϕ; the inner two have 256 sectors each, and the outer one has 512 sectors, but the wires in the outer chamber are ganged in pairs, so the total number of readout channels for all three TRD layers is the same. The radiator and the chamber are separated by a gap between two concentric Mylar windows. Dry CO_2 gas is flowing inside the gap in order to prevent the pollution of Xe mix with high-penetrating nitrogen gas. The outer window of a gap is aluminized and used as a drift chamber cathode (by keeping it at a negative -1 kV voltage). The windows

Parameter	Specification
Number of layers	3
Radius	$R_{in} = 17.5$ cm, $R_{out} = 49$ cm
Length total/active	188/167 cm
Total thickness	0.081 X_0 at $\eta = 0$
Transition radiation energy	< 30 keV
Radiator foils	393 foils, 18 μm thick polypropylene
Radiator/Gap/Chamber thickness	65/2/23 mm
Gas type	Radiator: N_2; Gap: CO_2; Chamber: 91% Xe+7% methane+2% ethane
Gas pressure	Radiator: 1.012 atm; Gap: 1.010 atm Chamber: 1.008 atm
Sense wire specifications	30 μm Au plated tungsten, at 90 g
Field wire specifications	100 μm Au plated Cu/Be, at 400 g
Grid wire specifications	70 μm Au plated tungsten, at 350 g
Wire voltage	Sense: +1.6 kV; Field: +0.2 kV Grid: grounded
Drift field	0.7 kV/cm
Drift velocity	25 μm/ns
Maximum drift time	0.6 μs
Number of sense wires/layer	256/256/512
Number of pads/layer	256/256/256
Total channels	3×256 (wires) + 3×256 (pads)

Table 3.4: Transition Radiation Detector selected parameters.

are kept cylindrical by maintaining a small pressure difference (≈ 2 mbar) of the three gas mixes used in the modules. Usage of both the time and charge information in the TRD gives a rejection factor of 50 against pions with 90%

efficiency for isolated electrons [57].

Some important parameters of the TRD are listed in Table 3.4 [57, 83].

3.4.3 Central Drift Chamber

The Central Drift Chamber (CDC) [84] of the DØ detector covers the pseudorapidity range $|\eta| < 1.2$ and provides crucial information about charged particle tracks in the central region. This information includes geometrical parameters of tracks and the ionization (dE/dx) on the track.

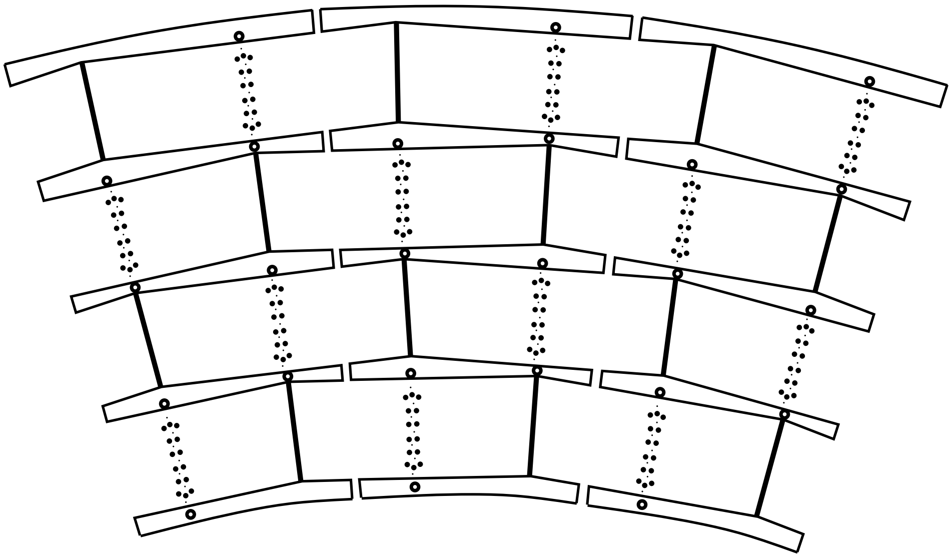

Figure 3.13: End view of a Central Drift Chamber section.

The CDC fills the space between the TRD and the CC cryostat (see Fig. 3.8). It consists of 4 concentric layers of drift cells, 32 cells per layer. Cells in adjacent layers are shifted in ϕ by one half cell for improved pattern recognition in the detector. Each cell has anode wires in the center and cathodes at cell boundaries (see Fig. 3.13). The 7 sense wires of a cell measure the

Parameter	Specification
Radius	$R_{in} = 49.5$ cm, $R_{out} = 74.5$ cm
Length	180 cm
Layers/sectors	4/32
Sense wires	7/cell, 896 total
Sense wire separation	6.0 mm radially, 200 μm stagger
Wire specifications	Sense: 30 μm Au plated W, 110 g tension Field: 125 μm Au plated CuBe; 670 g tension
Delay lines	2/cell, 256 total
Delay line velocity	2.35 mm/ns
Sense wire HV	+1.45 kV (inner), +1.58 kV (outer)
Gas type	93% Ar+4% CH_4 + 3% CO_2 + 0.5% H_2O
Gas pressure	1 atm
Gas gain	$2 \cdot 10^4$ (inner), $6 \cdot 10^4$ (outer)
Average drift field	620 V/cm
Average drift velocity	40 μm/ns
Total channels	$896 + 2 \times 256$
Position resolution	$r\phi$: 180 μm; z: 2.9 mm
Tracking efficiency	88% for isolated tracks

Table 3.5: Central Drift Chamber selected parameters.

drift time which is translated into the coordinate in $r - \phi$ plane. Sense wires are staggered by ± 200 μm for removing left-right ambiguities in hit positions. The z-coordinates are measured by two delay lines located just before the first and just after the last sense wire of a cell.

Mechanically, the CDC assembly is non-typical, since it consists of 32 free-standing modules (each of them in principle can be replaced). The modules are contained in a support cylinder with carbon fiber inner and 0.95 cm aluminium outer surfaces. The outer wall serves as a main support for the whole CDC. Each module is constructed of Rohacell foam covered with epoxy-coated Kevlar cloth and wrapped with a double-layer of 50 μm Kapton [57]. The G10 plastic endpieces hold wire plugs which match holes machined in the outer aluminium endcaps for precise wire positioning. The delay lines (magnetized wire wound around the carbon rods) are located into teflon tubes imbedded in the Rohacell foam. When the avalanche hits outer sense wires, it induces pulses on the delay lines, and the z-coordinate of the avalanche is measured by the difference in the pulse arrival times at the two ends of the delay line.

A single layer scintillating fiber detector with 128 individual fibers was installed on the CDC support cylinder for precise *in situ* calibration of the CDC drift velocities. It is described in detail in Ref. [85].

Major CDC parameters are listed in Table 3.5 [50, 57].

3.4.4 Forward Drift Chambers

The Forward Drift Chambers (FDC's) [67] extend the pseudorapidity coverage of the CDC up to $|\eta| < 3.1$. Two mirror-image chambers are located on the both sides of the VTX/TRD/CDC barrels before the EC cryostat (see Fig. 3.8). The inner FDC radius is 11 cm, and the outer radius of 62 cm is somewhat less than that for the CDC to allow passage of the cables connecting other central detectors.

Each FDC consists of three chambers (see Fig. 3.14) stacked along the

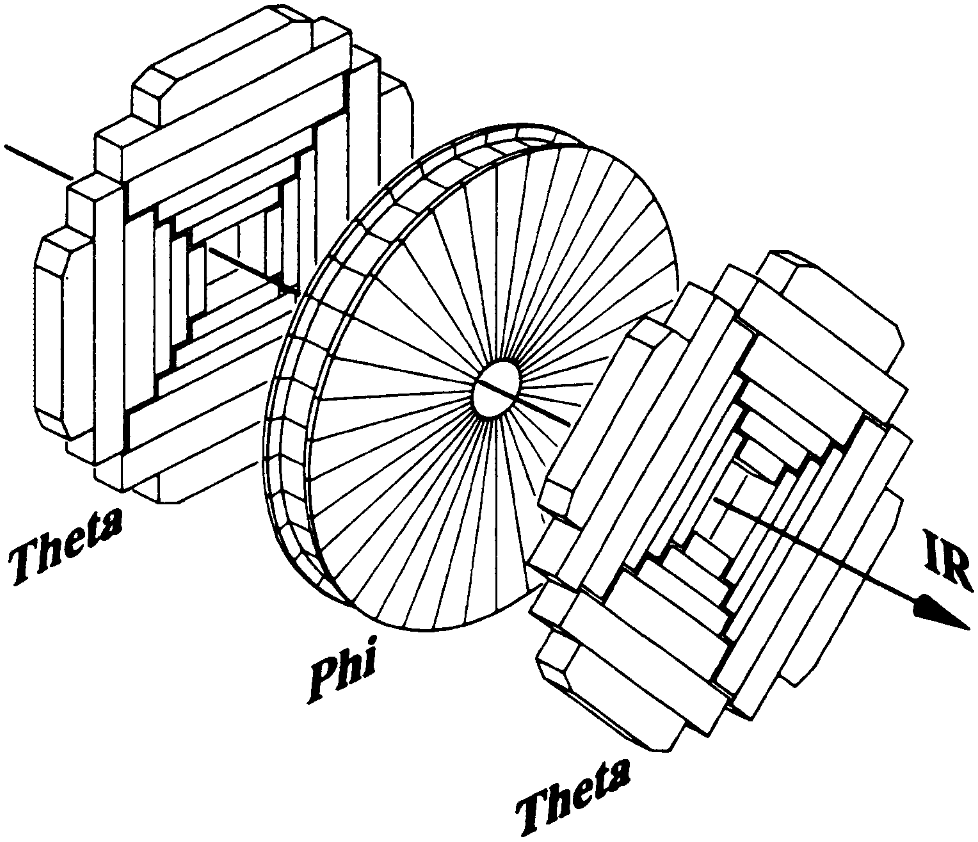

Figure 3.14: Forward Drift Chambers layout.

beam direction. The middle chamber (so called Φ-chamber) has radial wires and measures the ϕ-coordinates of the tracks. The outer two chambers (so-called Θ-chambers) have azimuthal wires and measure the polar angles of the tracks. The Φ-chamber is divided into 36 azimuthal sectors, with 16 sense wires each. The wires traverse the chamber plane along the radii, thus pointing toward the beam. Each Θ-chamber consists of four independent quadrants, each containing 6 rectangular cells at increasing radii. Each cell has 8 sense wires parallel to the beam direction. The inner 3 chambers are made of half-cells (so that electrons can drift only in one direction) which aids in resolving

Parameter	Θ-chamber	Φ-chamber
Radius	$R_{in/out} = 11.0/62.0$ cm	$R_{in/out} = 11.0/61.3$ cm
Position in $\lvert z \rvert$	$104.8 - 111.2$ cm $128.8 - 135.2$ cm	$113.0 - 127.0$ cm
Modules	4 quadrants of 6 layers	36 sectors
Sense wires	8 per cell, 192 total	16 per cell, 576 total
Sense wire separation	8.0 mm with 200 μm stagger	
Wire material/ tension	Sense: 30 μm Au plated W/$50 - 100$ g Field: 163 μm Au plated Al/$100 - 150$ g	
Delay lines	1 per cell, 24 total	none
Delay line velocity	2.35 mm/ns	N/A
Sense wire HV	+1.66 kV	+1.55 kV
Gas type	93% Ar+4% CH_4 + 3% CO_2 + 0.5% H_2O	
Gas pressure	1 atm	
Gas gain	Inner wires: $2.3 \cdot 10^4$ Outer wires: $5.3 \cdot 10^4$	$3.6 \cdot 10^4$
Average drift field	40 μm/ns	37 μm/ns
Maximum drift distance	5.3 cm	
Position resolution	≈ 300 μm	≈ 200 μm
Total channels	1×192 (wires) + 2×24 (delays)	1×576 (wires)
Efficiency	82% for isolated tracks	

Table 3.6: Forward Drift Chambers selected parameters.

left-right ambiguities. Adjacent sense wires of both Θ and Φ chambers are staggered by ± 200 μm for the same purpose. The outer Θ-chambers are rotated by $\pi/4$ one relative to the other for further improvement of pattern recognition. Each Θ-cell is equipped with one delay line (similar to ones used in CDC, see sec. 3.4.3) for measuring the z-positions of the hits.

The cell walls are made of G10 plastic or Kevlar coated Nomex covered with Kapton. As in the CDC, the cathodes are made of conductive strips attached to the walls of the supporting structure. Each cell of the Φ-chamber has a single field shaping wire; there are two analogous wires in the Θ-chamber cells. The FDC uses the same gas mixture as the CDC (see sec. 3.4.3).

The major parameters of both Θ and Φ chambers are listed in the Table 3.6 [50, 57, 67].

3.5 Muon System

Muons are highly penetrating particles, since they interact with matter only via electromagnetic or weak forces. Being heavy particles (if compared to electrons) they typically do not lose much energy via *bremsstrahlung* in the detector material; the energy loss mostly occurs due to the ionization of the detector media. Thus, muons with energy above a certain threshold ($\approx 3.5 - 5.0$ GeV) pass through the entire DØ detector. Therefore, the muon detection system is located outside the calorimeter, and it is well protected from the debris from the hadronic and electromagnetic showers by the massive calorimeter material (see sec. 3.3).

The DØ muon system consists of five separate solid-iron toroidal magnets and several multilayers of drift tube chambers. It covers the pseudorapidity range up to the very forward region ($|\eta| < 3.6$) (see Fig. 3.15). The central toroid (CF) (see Fig. 3.16) covers the pseudorapidity range $|\eta| \leq 1.0$, and

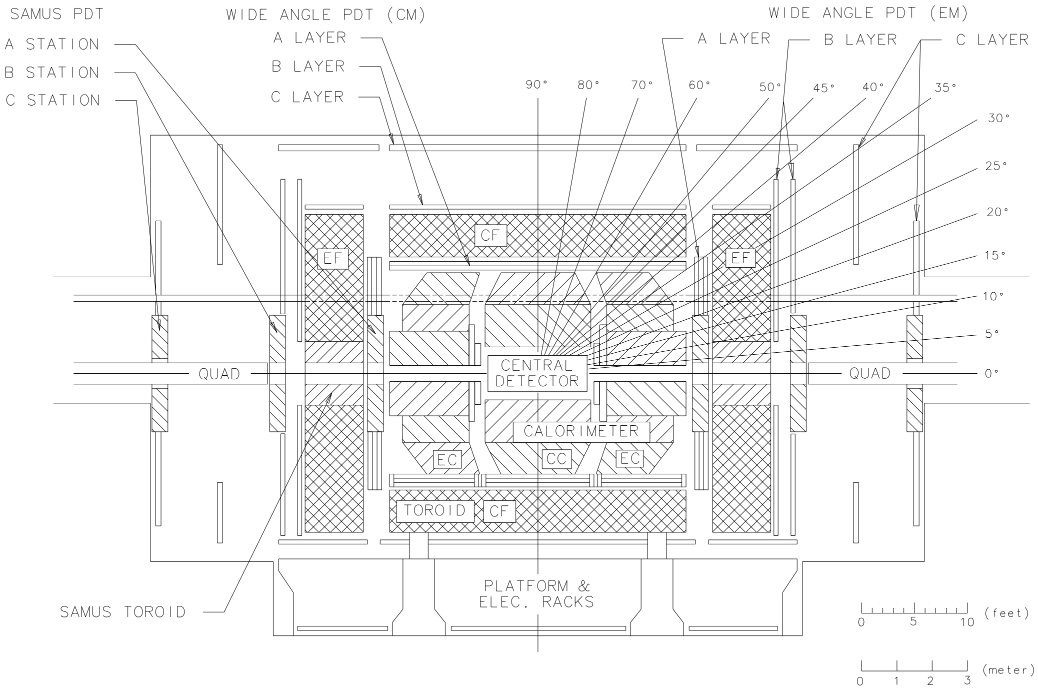

Figure 3.15: Muon System side view.

two end toroids (EF) extend the coverage to $|\eta| \leq 2.5$. They are the parts of the Wide Angle Muon System (WAMUS). The Small Angle Muon System (SAMUS) differs from the WAMUS. The two SAMUS toroids fit the holes in the EF toroids and cover the rest of the pseudorapidity range above. The magnetic field in the toroids varies across the square cross section, peaking at about 2 T. The field lines are azimuthal so that muon tracks are bent in the $r - z$ plane. Muon reconstruction uses a precise field map obtained by special pre-run measurements. The thickness of the calorimeter and toroid material (expressed in the interaction lengths) as a function of the polar angle θ is shown in Fig. 3.17.

The muon system readout electronics is mainly located on the chamber modules. Signal shaping, time-to-voltage conversion, chamber monitoring and

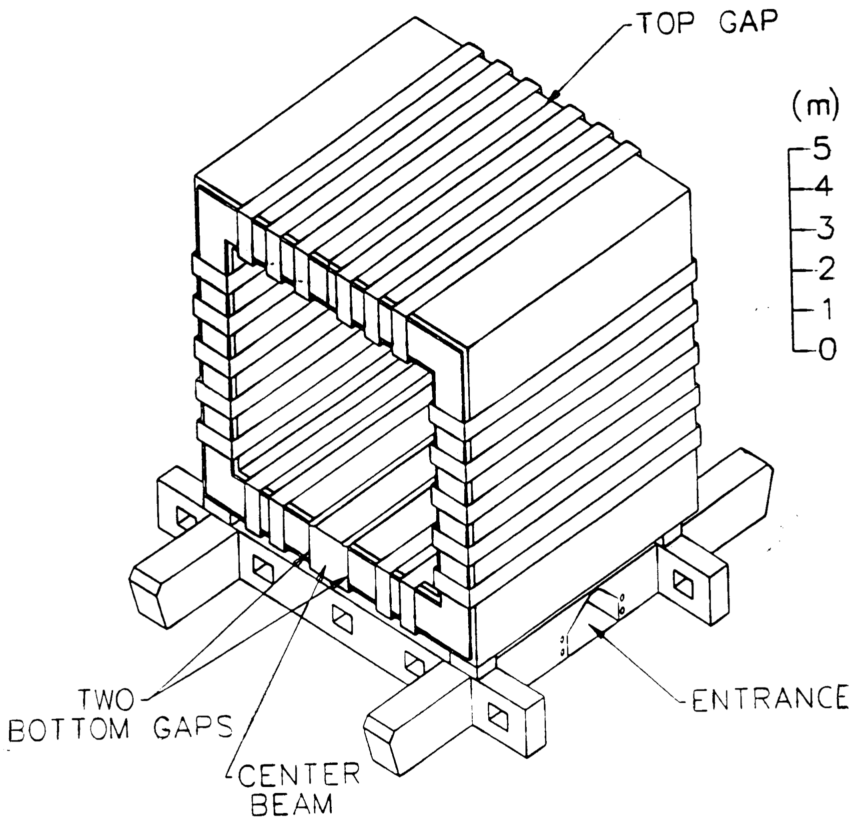

Figure 3.16: Muon System CF toroid.

signal multiplexing is done locally, while the digitizing and the trigger electronics reside outside the detector. Each electronic module processes signals from 6 adjacent drift cells. Digitizing of the muon signal is done with the 12-bit ADC's, analogous to those used in the calorimeter electronics (see sec. 3.3). There is a total of 50,920 analog channels in the system. As for the calorimeter case (see sec. 3.3.2), the coarse information about the muon event is passed to the Level 1 trigger using one latch bit per each PDT (see sec. 3.6). The Level 1/1.5 muon trigger uses the locations of the hit tubes for a coarse estimation of the number of muon candidates and their transverse momenta.

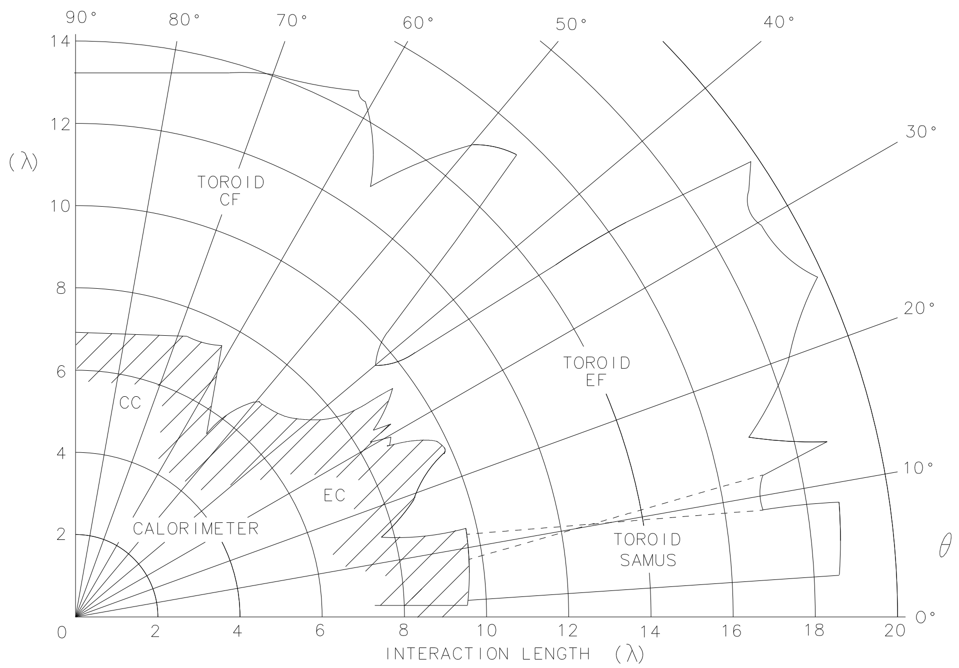

Figure 3.17: Amount of calorimeter and muon toroid material as a function of the polar angle.

The following sections discuss details of the SAMUS and WAMUS detectors.

3.5.1 Wide Angle Muon System

The Wide Angle Muon System (WAMUS) [86] provides measurements for all muons crossing the CF toroid and for most of the muons traversing the EF toroids. It covers the pseudorapidity range $|\eta| \leq 1.7$, and consists of 164 proportional drift tube chambers (PDT's) with chamber wires oriented along the magnetic field lines. The PDT's are grouped into 3 superlayers. The innermost, A-layer, is located inside the toroidal magnets, and the two outer layers, B and C, surround the magnet (see Fig. 3.15). The A-layer has four planes of PDT's; the B- and C-layers have three planes each. The PDT planes are shifted relative to each other in order to resolve left-right ambiguities as shown in the end view of a typical three-plane layer (see Fig. 3.18). There is a total of 11,386 PDT's in WAMUS. The WAMUS chambers are grouped into 8 sections (octants) in ϕ for triggering purposes.

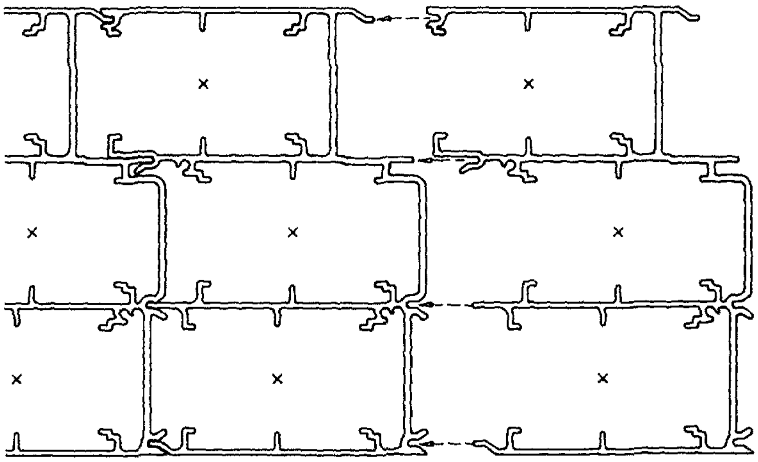

Figure 3.18: End view of a WAMUS chamber assembly.

An approximate drift field map in a single PDT is pictured in Fig. 3.19. The active volume of each PDT measures 102×55 mm^2. The cathode pad strips are located at the top and bottom of the tubes, and a single 50 μm anode wire is situated in the cell center. The anode wires and cathodes are held at $+4.56$ kV and $+2.3$ kV, respectively, with aluminium PDT walls being grounded. Tubes are filled with an $Ar/CF_4/CO_2$ gas mixture which yields 65 μm/ns drift velocity. The maximum drift distance is 5 cm. The coordinate in the direction of the wires (non-bend view) is measured with the cathode

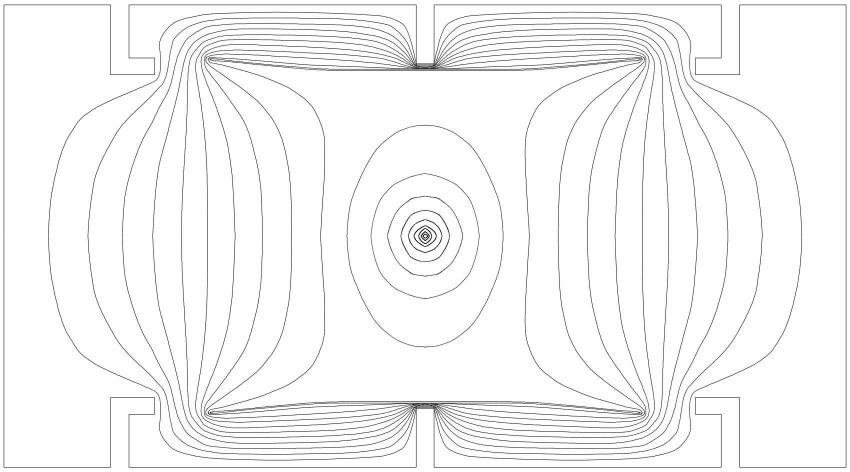

Figure 3.19: Drift field map in a WAMUS cell.

pads and using the timing information from the wires. (The wires of adjacent cells are jumpered at one end, and the signals are read out from the other end, which allows to measure a coarse hit position by the difference in the arrival times.)

The position resolution is 1.6 mm along the wires and 0.53 mm in the drift plane [57]. The muon momentum resolution of the WAMUS can be approximately described as [57]:

$$\left(\frac{\sigma(\frac{1}{p_\mu})}{\frac{1}{p_\mu}}\right)^2 = 0.18^2 + (0.01 \cdot p_\mu[\mathrm{GeV}/c])^2. \qquad (3.6)$$

It is asymmetrical in p_μ because the momentum is calculated from the inverse of the track saggita. Some of the WAMUS parameters are listed in Table 3.7.

Parameter	WAMUS	SAMUS
Rapidity coverage	$\|\eta\| \leq 1.7$	$1.7 \leq \|\eta\| \leq 3.6$
Magnetic field	2 T at maximum	2 T at maximum
Number of chambers	164	6
Interaction lengths	13.4	18.7
Gas type	90% Ar/5% CF_4/5% CO_2	90% CF_4/10% CH_4
Avg. drift velocity	65 μm/ns	97 μm/ns
Anode wire voltage	+4.56 kV	+4.0 kV
Cathode pad voltage	+2.3 kV	N/A
Number of PDT's	11,386	5,308
Bend view resolution	$\pm$0.53 mm	$\pm$0.35 mm
Non-bend resolution	$\pm$3 mm	$\pm$0.35 mm

Table 3.7: Muon system characteristics.

3.5.2 Small Angle Muon System

The Small Angle Muon System (SAMUS) [87] is not used for the analysis discussed in this work, so we give only a brief description of this detector. The SAMUS system also have three superlayers of PDT's. However, the higher occupancy of the forward region requires smaller PDT's. They are made of stainless steel tubes (3 cm in diameter) filled with CF_4/CH_4 gas mixture which yields a drift velocity of 97 μm/ns. The maximum drift time is 150 ns. Like in the WAMUS case, the A-layer is located inside the toroid, while B- and C-layers are mounted outside. Each layer has three planes of PDT's oriented in x, y, and u-directions (the u-direction is rotated by 45° degrees with respect to the x and y axes). There is a total of 5,308 PDT's in SAMUS [57].

The position resolution in a single drift tube is 0.35 mm. Some of the important SAMUS parameters are listed in Table 3.7 [57].

3.6 Trigger and Data Acquisition

But we stuck to our starboard triggers

Though we yawned like dying cod.

Raymond Asquith, Letter, 4 March, 1900

The DØ detector works in a high-luminosity environment with a large number of particles traversing its active volumes for each collision. However, only a tiny fraction of events are of physics interest. In order to uncover these valuable events from the huge background of primarily elastic or minimum bias $p\bar{p}$ interactions, the DØ detector uses a complex multilevel trigger [57].

The DØ trigger framework is organized into 3 main levels of increasingly sophisticated event selection (see Fig. 3.20). The scintillator-based hardware Level 0 trigger deals with all $p\bar{p}$ collisions (which occur with a typical rate of 350 kHz at $5 \cdot 10^{30}$ cm^{-2}s^{-1} luminosity), and detects the occurrence of an inelastic collision. It reduces the input rate by about a factor of 3. The Level 1 triggers are based on hardware elements arranged in a flexible architecture via software specifications. Many of the Level 1 triggers operate within 3.5 μs time interval between bunch-crossings, thus contributing nothing to the deadtime (see Chapter 4). They typically slow down the counting rate to 200 Hz. Others require several bunch-crossing times for decision making and are referred to as Level 1.5 triggers. The Level 1.5 triggers suppress the event rate by an

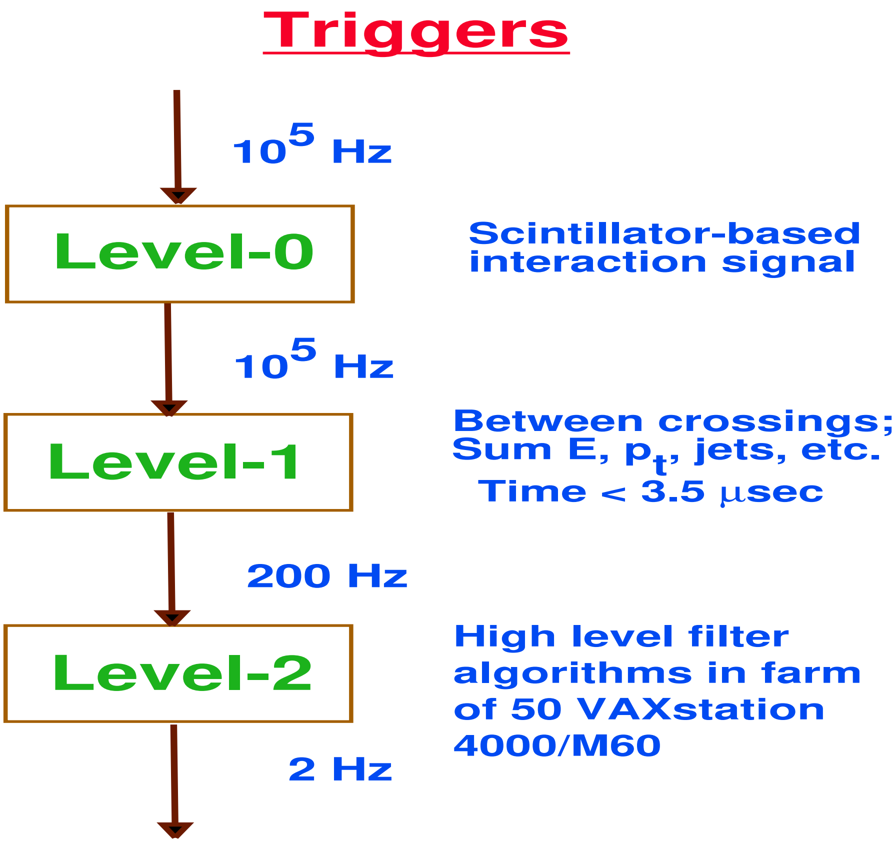

Figure 3.20: Trigger organization and typical trigger rates.

additional factor of 2. The output of Level 1 and Level 1.5 triggers is fed into the standard DØ Data Acquisition (DAQ) System and passed to the last, Level 2, trigger. The Level 2 trigger is software based. The event selection is done by a microprocessor farm which performs a coarse reconstruction of the event parameters, and uses calorimeter and tracking information for decision making. The events which pass at least one out of a broad collection of the Level 2 triggers are passed to the host computer (with a typical rate of 2 Hz) for recording and monitoring. A simplified block-diagram of the Level 2 trigger and DAQ system is shown in Fig. 3.21.

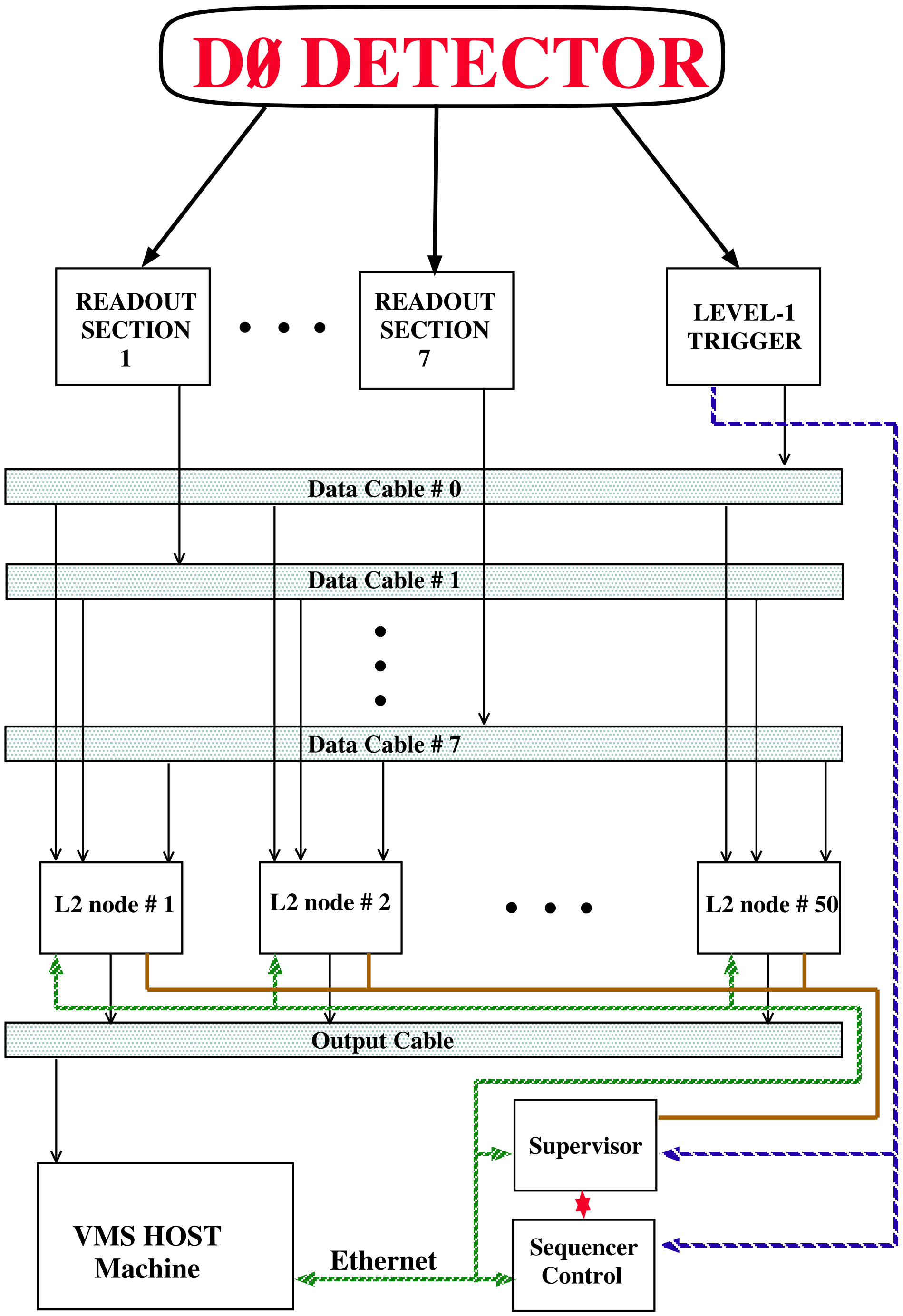

Figure 3.21: A simplified view of the Level 2 trigger and Data Acquisition System.

3.6.1 Level 0 Trigger

The Level 0 trigger [88] detects inelastic collisions and also serves as a luminosity monitor for the experiment (see sec. 3.6.7). The trigger is based on two scintillating hodoscopes mounted on the front surfaces of the EC's (see sec. 3.3). The hodoscopes have a partial coverage for the pseudorapidity range $1.9 < |\eta| < 4.3$, and a full coverage for $2.3 < |\eta| < 3.9$. The trigger is $\approx 99\%$ efficient for non-diffractive inelastic collisions. The Level 0 trigger also roughly measures the z-position of the interaction vertex by the time difference of the signals in the two hodoscopes. The z-position is then used by the Level 1 trigger for correcting the transverse energy. The vertex position resolution is $\sigma_z \approx 3.5$ cm for single interaction events and ≈ 6 cm for the case of multiple interactions [88]. A cut on the vertex position ($|z_{vtx}| < 100$ cm) is made at the Level 0 in order to separate $p\bar{p}$ collisions from the beam interactions with the residual gas. The Level 0 trigger also marks the event as a single or multiple interaction according to the spread of the signal arrival times in each hodoscope. The Level 0 trigger decision making is done completely by hardware. A rough vertex position (the so called "fast vertex") is measured within 0.8 μs after the interaction, and more precise ("slow vertex") information is available within 2.1 μs.

3.6.2 Level 1 Trigger

The Level 1 trigger [89] logic uses several inputs: Level 0 information, Level 1 Calorimeter trigger, Level 1 Muon trigger, Level 1 TRD trigger (the latter was not used in run Ia), and certain timing information, as shown in Fig. 3.22. Typical output of the Level 1 Calorimeter and Muon triggers is the number of struck trigger towers (see sec. 3.3.2), the transverse energy deposited in these towers, and the number of muon candidates and their p_T (see sec. 3.5). These quantities are fed into the Level 1 trigger framework which is based on the two-dimensional AND–OR network, which converts up to 256 inputs into a 32-bit word with the Level 1 trigger information. An event passes the Level 1 trigger if at least one bit of the trigger word is set.

Some of the Level 1 bits were prescaled, which means that they were set for only every k-th event which passes the corresponding path of the logical network. The numbers k are different for different bits and in general depend on the luminosity. The prescale technique makes it possible to collect samples of events corresponding to large cross section processes, such as multijet production, minimum bias events, etc. Without such a prescale these events would simply oversaturate the trigger and DAQ system bandwidths making the detector incapable of collecting rare and more interesting data. More flexible, Level 2 prescales are used in run Ib, allowing for unprescaled Level 1 triggers (see sec. 3.6.4).

Additional information used by the Level 1 trigger is the Main Ring activity (see sec. 3.1). Since the Main Ring of the Tevatron passes through the DØ detector and continuously operates during the collider run for stacking antiprotons, caution must be used when collecting the data during the Main Ring activity periods.

There are two trigger terms which were used during run Ia for vetoing

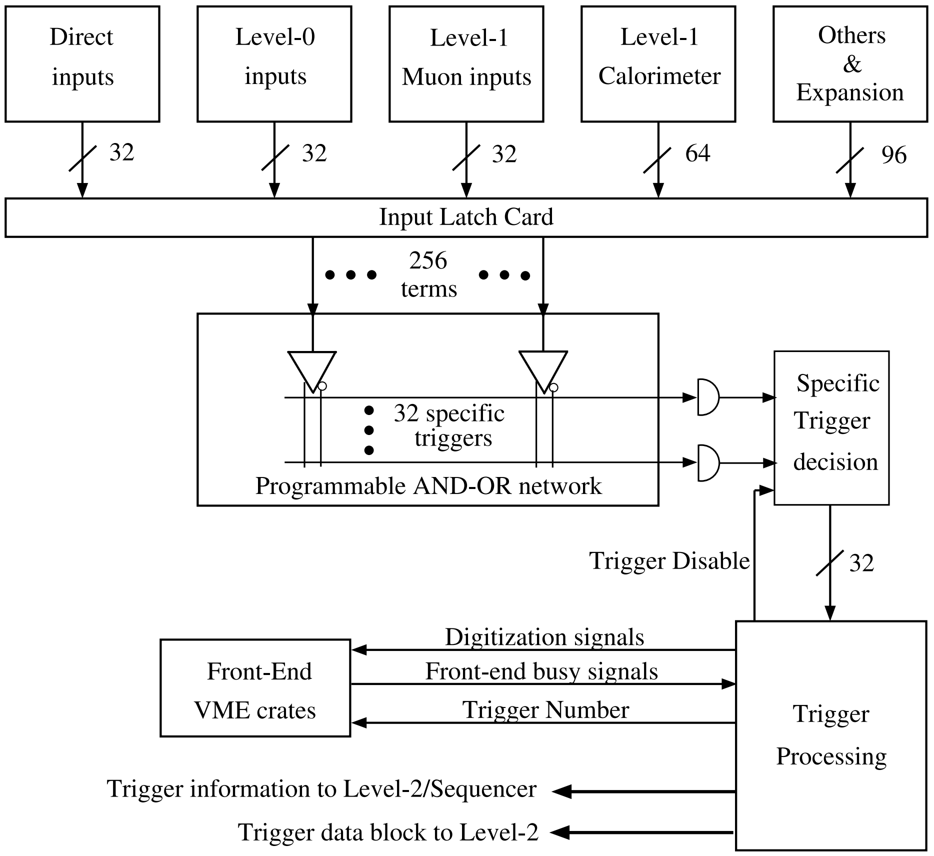

Figure 3.22: A block-scheme of the Level 1 trigger.

events which are likely to be contaminated by the Main Ring beam debris [90]. The first one is the MRBS_LOSS gate with a duration of 0.4 s which occurs during the Main Ring injection and transition, when the activity around the Main Ring results in a high noise in the DØ muon system and calorimeter. Most of the Level 1 triggers do not collect data during this gate. Since Main Ring injection/transition occurs every 2.4 s, the average dead time due to the MRBS_LOSS gate is about 17%. The second type of the Main Ring vetos is the so-called microblanking signal, which is generated if the Main Ring bunches pass through the DØ detector during ± 800 ns livetime of the muon system, centered on the Tevatron bunch-crossing.

Typically, the Level 1/1.5 muon triggers reject events if the microblanking signal is present. Calorimeter based Level 1 trigger still collect the data during the microblanking period, however the quality of this data is rather low, and it is normally rejected during the offline event selection by physics analyses which deal with rare events. Therefore, microblanking contributes $7-9\%$ to the detector deadtime. The total deadtime due to the Main Ring activity is about 25%, and thus quite significant. It was decreased by a factor of 2 in run Ib using the so-called active veto technique [91].

More details on the Level 1 trigger can be found in Refs. [57, 89].

3.6.3 Data Acquisition System

Once an event passes the Level 1 trigger, it is fed into the DØ Data Acquisition (DAQ) System [92] for further analysis by the Level 2 software trigger (see sec. 3.6.4). The system is based on a farm of 48 parallel nodes connected to the detector electronics and triggers via 8 high-speed 32-bit data busses. Each node has a VAXstation 4000-60 or 4000-90 processor (with memory board) connected to a multiport memory used for data exchange via VME bus. The fully digitized data from the calorimeter, CD, muon detector, and Level 0/1 triggers appear in the output buffers of approximately 80 VME crates with ADC's and FADC's about 1 ms after the receipt of the Level 1/1.5 trigger. Each crate prepares compressed information from its modules in a 512 kByte memory module controlled by VME Buffer Driver board which is capable of transferring the data via one of the high-speed busses at a rate of 40 MBytes/s. Each of the 8 busses is used for a particular subdetector or trigger.

The operation of the DAQ system is under the control of the Level 2 trigger supervisor processor, which initiates the data transfer from the VME crates to the multiport memory, and picks a node for the event processing (see Fig. 3.21). Each node has an identical copy of the Level 2 filtering software developed using high-level languages (FORTRAN, C, PASCAL).

Upon reaching the Level 2 nodes, the raw detector data is converted in ZEBRA [93] format, which allows dynamic data structuring and stores information of different types in form of data banks. This format is used in all subsequent data processing (see sec. 3.6.5), and is a standard within DØ.

3.6.4 Level 2 Trigger and Online Processing

The software event filtering performed by the 48 Level 2 trigger nodes (see sec. 3.6.3) reduces the input Level 1/1.5 rate of $\approx$ 200 Hz to 2 Hz output rate for the data. The filtering software performs a coarse reconstruction of the event parameters and then compares the event characteristics with a set of software-defined Level 2 trigger masks, depending on which particular Level 1 trigger bits were set. As a result, certain Level 2 bits (out of a total of 128 available) are set. A typical Level 2 trigger accepts events which satisfy certain requirements on the transverse energies of the electromagnetic/hadronic jets, number and transverse momenta of muons, missing transverse energy in the event, etc. Some of the Level 2 bits are prescaled in run Ib (see sec. 3.6.2 for prescale definition), thus allowing for usage of the unprescaled Level 1 triggers.

If at least one of the Level 2 bits is set, the event passes the Level 2 trigger, and is temporarily written on disk, and then transferred to 8 mm magnetic tape cartridge (Exabyte format) for further offline processing. All the events which pass Level 2 trigger are combined into the so-called ALL data stream; the events of a particular interest ($\approx 10\%$ of the ALL stream) which pass a certain set of the Level 2 triggers are also copied into an express-line stream (EXP) for immediate reconstruction and analysis. A small fraction of the events ($\sim 1\%$) is fully reconstructed online for the physical and technical monitoring purposes. This is done with the EXAMINE package [94] which runs separately for each sub-detector, and for global monitoring.

A typical event processing time in Level 2 trigger is less than 200 ms, which comfortably meets the Level 1/1.5 output bandwidth.

3.6.5 Offline Reconstruction

The preliminary reconstruction of the event which is done at the Level 2 trigger provides only coarse parameters of the event. The Level 2 timing requirements do not allow for a more thorough reconstruction. The complete event reconstruction is therefore done offline on the fast UNIX farm based on Silicon Graphics processors with a special package named DØRECO [57]. The DØRECO code was continuously improved throughout run Ia, so the data was originally reconstructed by a mixture of different versions of this package.

After the end of run Ia, the whole data set was reprocessed with the latest available version of DØRECO (v.11).

The DØRECO package uses the raw detector data stored in ZEBRA banks by the DAQ system (see sec. 3.6.3) as well as detector and enviromental information (detector surveys, calibration constants, etc.) stored in separate databases as an input. There are two output streams produced by the reconstruction program: the STA stream and the DST stream. The STA (STAndard) output contains raw detector information and various additional ZEBRA banks created by DØRECO during the full event reconstruction, such as banks with reconstructed hits, tracks, calorimeter clusters, identified particles, etc. The STA output files are typically large ($\approx$ 600 kBytes/event) and therefore used only at the final event selection stages, when the number of candidate events is small — typically for event display purposes. The DST (Data Summary Tape) stream contains a reduced version of the STA data. All raw detector data and most of the banks created on the intermediate reconstruction stages (such as hit-finding) are dropped. Only the physics information such as kinematical parameters of the identified particles and jets, compressed calorimeter information, and all parameters relevant to the missing transverse energy calculations are kept for the DST stream. The size of the DST files is approximately 50 times smaller than the STA output, which makes it possible to keep a significant sample of the events on the computer disks for fast physics analysis. At the same time, the information contained in the DST files is sufficient for application of most of the offline selection criteria, like the ones described in Chapter 4.

Details of the particle assignment, jet reconstruction, missing transverse energy calculations, etc. can be found in Chapter 4 and in Refs. [50, 69, 95].

3.6.6 High Voltage Power

All DØ subdetectors use standard High Voltage (HV) power supplies. A special VME based and computer controlled HV system [96] was developed for the DØ detector. Each VME crate contains 6 power supplies (modules) controlled by a Motorola 68020 microprocessor. Three different modules are used in DØ: negative and positive supplies with the voltage of 10 V to 5.6 kV (in 1.36 V increments) at maximum current of 1.0 mA, and positive supplies with the voltage of 10 V to 2.0 kV (in 0.49 V increments) at 3.0 mA maximum current.

The system is controlled and monitored by the host computer capable of changing the operational voltages on different subdetectors and monitoring the HV trips initiated by over-current or over-voltage. A special package for high-level monitoring and quick setting of different operational parameters of the HV system is used for HV control during the data taking. The system is capable of keeping the HV within 0.5 V of the desired value.

For more details on the DØ HV system see Ref. [57].

3.6.7 Luminosity Monitoring

The instantaneous luminosity monitoring is an important issue for any collider experiment, since precise cross section measurements completely rely on the known integrated luminosity of the data sample.

The DØ detector uses the rate for non-diffractive inelastic collisions for luminosity monitoring. This information is provided by the Level 0 scintillating hodoscopes (see sec. 3.6.1). Several corrections to the raw counting rate of the hodoscopes are applied in form of the so-called scalers at Level 1 trigger. Each of a total of 6×32 scalers correspond to one out of 6 possible bunch-crossings, and to one out of 32 possible Level 1 trigger bits. The scalers take into account the multiple interaction factor, the experimental dead time, possible Level 1 trigger prescales, the Main Ring activity veto (see sec. 3.6.2), and others corrections. See Ref. [97] for details.

The calibration of the luminosity monitor is based on the world average values of the total, elastic, and single diffractive cross sections, using the results from CDF [98] and E710 [99]. We use the average of 58.9 pb for inelastic and 9.5 pb for single diffractive cross sections [100]. The systematic error of the normalization constant is 12%. The major sources of systematics are the uncertainties in the efficiency and cross section measurements. It expected to be reduced in run Ib.

The values of the instantaneous luminosity are in agreement with the accelerator division information, based on the measurements of the beam current in the accelerator and on other store parameters [101]. However, this information is available only when beam conditions are stable, and it does not have all the DØ-specific corrections, therefore it can not be used for trigger-dependent luminosity calculations.

3.7 Monte Carlo

The comparison of the observed $Z\gamma$ signal with the SM predictions and the derivation of the limits on anomalous couplings rely very much on dependable and precise Monte Carlo calculations. There are several requirements which a Monte Carlo event generator must satisfy.

First, the generator should take into account the interference effects between production, trilinear, and decay diagrams and be capable of calculating total and differential cross sections of the reaction (2.7) for both the SM and anomalous cases. Second, the generator must simulate response of the different parts of the DØ detector and take into account various particle identification efficiencies, trigger effects, etc. And third, the generator must be capable of producing a large number of events fast. The last requirement is essential because anomalous effects are pronounced only at high p_T^γ, where the SM cross section is very small, and in order to make a precise fit of the p_T^γ spectrum (see sec. 5.2) one needs a significant number of events generated in the high photon transverse momentum region, which corresponds to thousands of the events in the whole phase space used for the analysis. Such a huge event sample should be generated many times for different values of couplings in order to derive the limits. And still more events need to be generated to optimize the set of cuts and derive systematic errors.

Currently there are two event generators which have $Z\gamma$ matrix elements incorporated. The first one is PYTHIA [102] which is capable of generating only SM $Z\gamma$ events. Unfortunately, it does not properly take into account the effects of the finite Z width and the interference between initial and final state radiation diagrams (see Fig. 2.2). Therefore, it fails the requirements listed above. The second generator by U. Baur and E.L. Berger [20] (in what follows called BAUR[2]), briefly described in 2.3.3, does have a full set of matrix elements necessary for the calculations of the processes (2.7), (2.9), and the capability to calculate the contribution of anomalous couplings. However, the detector simulation part of the original generator is rather simple and does not take into account hadronization effects, and the underlying event structure, as well as fine details of the DØ detector.

There are two options for incorporating the instrumental effects into the event generator. The first is simply to use the output of the BAUR generator (4-momenta of the final state particles) as an input for a comprehensive DØGEANT detector simulation program [103]. The overlap with the underlying event and conversion of the data into the GEANT format in this case can be done by means of the ISAJET event generator [104], which is a standard tool within DØ. However, the generation of thousands of events with the GEANT detector simulation is a very resource-consuming and slow task. Besides, it relies very much on a precise description of different detector components, which is not always in agreement with the measurements based on real data. Instead, we decided to use the other option and modified the original BAUR code to include a fast "toy Monte Carlo" simulation of the DØ detector as a part of this generator. Such a modified code in what follows will

[2] Authors' permission obtained.

be called DØBAUR.

The instrumental resolutions, particle identification efficiencies, trigger turn-on curves, and other crucial detector-specific parts of the fast simulation, are wherever possible based on data collected in the same run. Usage of the data-based numbers also takes into account the effects of the multiple interactions, underlying event, etc. Most of the efficiencies will be discussed in detail in Chapter 4, so here we will just list the main effects which were taken into account.

- Smearing of electron/photon and muon momenta as well as the missing transverse energy according to the resolutions (3.3), (3.6), and (3.5), respectively.

- Primary vertex longitudinal position displacement ($z^0_{vtx} = -11.0$ cm) and smearing ($\sigma_z = 29.0$ cm).

- Photon, electron, and muon identification efficiencies (see sec. 4.1 for details).

- Photon losses due to conversions in the material in front of the calorimeter and random track overlap (see sec. 4.1.2).

- Level 1 and 2 trigger efficiencies and turn-on effects (see sec. 4.2 and 4.3).

- Geometrical acceptance and CC/EC gap effects (see sec. 3.3).

- Transverse kick of the $Z\gamma$ system due to the associated jet production. The transverse momentum of the $Z\gamma$ system is generated according to the observed Z boson p_T distribution [105]. Presently, no complete theoretical calculation of the $Z\gamma$ p_T distribution (including soft gluon resummation effects) exists. However, the shape of the $Z\gamma$ transverse momentum distribution is expected to be similar to that in the Z boson production.

The code was transported and primarily used on DEC Alpha platforms which allows for a fast generation of high-statistics samples. The standard output of the generator is a total cross section within the cuts and a set of histograms with different kinematical distributions, like those shown in Figs. 2.3 – 2.7. An interface for writing out unweighted events for further processing with DØGEANT was also incorporated into the code for future studies of the detector response. Additionally, the program has a flag which allows for the choice between the muon and electron channels during the simulation.

An important question is the systematic error on the calculated cross section. Several different uncertainties contribute to this error. They are summarized in Table 3.8 for the electron and muon channels.

The sources of the detector related uncertainties are described in detail in Chapter 4. The momentum smearing error was calculated by varying the smearing parameters by $\pm 1\sigma$. For the muon channel the uncertainty also accounts for different smearing parameters for the low and high $\int B\,dl$ muons (see sec. 4.3).

The major source of theoretical uncertainties is due to different possible choices for the structure functions. We choose the MRSD$-'$ [29] set of the next-to-leading logarithmic (NLL) order structure functions, because they describe the recent measurements of the W-decay asymmetry [106] as well as other electroweak phenomena better than the other sets of structure functions. We calculated the SM cross section for both channels with 21 different NLL and leading order (LO) structure functions [107]. After neglecting the old and outdated structure functions which contradict other experimental results, we estimated the scattering of the results, and ended up with $\pm 6\%$ estimate on the cross section uncertainties. The band obtained also covers the predictions

Source of error	Systematic uncertainties	
	Electron channel	Muon channel
Detector related errors		
Photon ID efficiency	7%	7%
Dilepton ID efficiency	5%	8%
Trigger efficiency	1%	8%
Random track overlap	1%	1%
Momentum smearing	1%	5%
Theoretical errors		
Structure function choice	6%	6%
Structure function scale	1%	1%
$p_T^{Z\gamma}$ effect	3%	3%
Total	11%	16%

Table 3.8: Sources of the systematic uncertainties in the cross section predictions, as calculated by the DØBAUR generator.

of another popular set of the structure functions by CTEQ [108]. The difference between the cross sections calculated using various structure functions is shown in Fig. 3.23. As is clear from this figure, LO structure functions result in a systematically lower cross section, if compared to the NLL structure functions. The Monte Carlo calculations in the DØBAUR code are based on

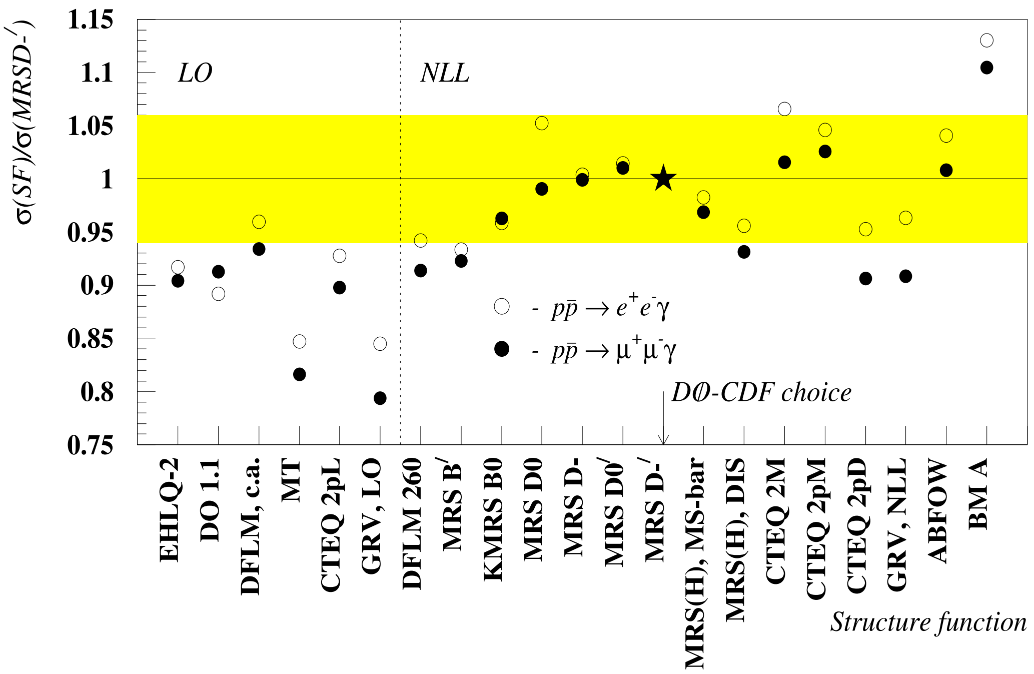

Figure 3.23: SM cross section of reactions (4.1) (open dots) and (4.2) (solid dots) for various sets of structure functions, normalized to that for the MRSD$-'$ set (DØ and CDF default set of structure functions for W/Z-physics, shown with the star). The shadowed band shows the $\pm 6\%$ systematic uncertainties which account for the cross section variations for different sets. Points to the left (right) of the dotted line correspond to LO (NLL) structure functions. Notations for the structure functions are given in Ref. [107].

the LO matrix elements (a full NLL calculation of $Z\gamma$ production, including anomalous $ZV\gamma$ couplings is presently not available). NLL QCD corrections are approximated by a k-factor (see sec. 2.3.3 and 2.3.4), so usage of NLL structure functions is more appropriate [35].

Another type of the theoretical uncertainty is the scale used for the structure function calculations. The error due to different scale definitions was estimated to be $\pm 1\%$ by varying the scale from the nominal value of $Q^2 = \hat{s}$ to $\hat{s}/2$ and $2\hat{s}$. Finally, the effect of the transverse kick of the $Z\gamma$ system due to the associated jet production was studied. It contributes less than 3% to the cross section uncertainty. The error originating from the p_T kick partially reflects the remaining uncertainty from QCD corrections beyond the NLL approximation.

Overall uncertainties in the cross sections for typical cuts (see sec. 4.2 and 4.3) and after the detector response simulation, as calculated by the DØBAUR Monte Carlo, are 11% for $e^+e^-\gamma$ and 16% for $\mu^+\mu^-\gamma$ cases. Combining the two channels, the error is 13%.